

ULTRAFAST PHOTOLUMINESCENCE FROM
POLY(*p*-PHENYLENEVINYLENE)

by

Murray McCutcheon

B. Sc. University of British Columbia, 1997

A THESIS SUBMITTED IN PARTIAL FULFILLMENT OF

THE REQUIREMENTS FOR THE DEGREE OF

MASTER OF SCIENCE

in

THE FACULTY OF GRADUATE STUDIES

DEPARTMENT OF PHYSICS AND ASTRONOMY

We accept this thesis as conforming
to the required standard

THE UNIVERSITY OF BRITISH COLUMBIA

September 1999

© Murray McCutcheon, 1999

In presenting this thesis in partial fulfilment of the requirements for an advanced degree at the University of British Columbia, I agree that the Library shall make it freely available for reference and study. I further agree that permission for extensive copying of this thesis for scholarly purposes may be granted by the head of my department or by his or her representatives. It is understood that copying or publication of this thesis for financial gain shall not be allowed without my written permission.

Department of Physics and Astronomy

The University of British Columbia

6224 Agricultural Road

Vancouver, B.C., Canada

V6T 1Z1

Date:

September 21, 1999

Abstract

Femtosecond time-resolved photoluminescence spectroscopy is used to study the dynamics of poly(*p*-phenylenevinylene) (PPV) at 77K and 300K over an energy range 2.19-2.37 eV. At all emission energies studied, the photoluminescence excited by ~ 100 fs long pulses of 400 nm radiation rises to a maximum value in less than 1 ps and then monotonically decreases with increasing delay. The decay curves can all be described by the summation of two, or in some cases three, exponential functions. Analysis of the spectral dependence of the various time constants extracted from these fits indicates that the photoluminescence at any given wavelength is due in general to the superposition of three transitions emanating from a single set of inhomogeneously broadened excitons. The three distinct transitions correspond to processes in which two, one or zero phonons are excited in the host polymer during the emission event. A complete analysis of the data indicates that the lifetime of the inhomogeneously broadened excitons is found to increase monotonically from a value less than the 300 fs time resolution of our system at 330 meV above the peak in the density of states (DOS), to 116 ps at an energy 7 meV below the peak in the DOS.

Table of Contents

Abstract	ii
Table of Contents	iii
List of Figures	vi
Acknowledgements	viii
1 Introduction	1
2 Theory	5
2.1 Introduction	5
2.2 Second Harmonic Generation	7
2.3 Sum Frequency Generation	11
2.4 Angle of Acceptance	14
2.5 Upconversion efficiency	17
3 Experiment	22
3.1 System Overview	22

3.2	Photon counting and data acquisition	26
3.3	Alignment	27
3.3.1	General	27
3.3.2	Acceptance angle considerations	28
3.3.3	Imaging	29
3.3.4	Laser upconversion	30
3.3.5	Alignment of collection optics	33
3.4	Sample Preparation	38
3.4.1	Monomer purification	38
3.4.2	Precursor polymerization	38
3.4.3	Thin film preparation	39
3.5	Data collection	39
4	Results and Discussion	41
4.1	CW spectra	41
4.2	Time resolved spectra (77 K data)	44
4.3	Time resolved spectra (300 K data)	49
4.4	Context	49
4.5	Interpretation	53
5	Conclusions	60

References **63**

Appendix A Phasematching Code **65**

List of Figures

1.1	Chemical structure of PPV	1
2.1	Time resolved luminescence spectroscopy	7
2.2	Index surfaces for the ordinary and extraordinary surfaces	10
2.3	Nonlinear crystal axes	11
2.4	Excitation and collection of luminescence	14
2.5	Phase matching detail for sum frequency generation	15
2.6	Half-angle of acceptance	16
3.1	Experimental set-up	23
4.1	Photoluminescence spectrum of a thin film of PPV	42
4.2	Temperature dependence of PPV photoluminescence	43
4.3	Short time regime of upconverted PPV luminescence at 77K.	45
4.4	Intermediate time regime of time resolved PPV luminescence at 77K.	46
4.5	Long time scale regime of upconverted PPV luminescence at 77K.	47
4.6	Slow and fast time constants extracted from the biexponential fits at 77K.	48
4.7	Luminescence transients at 300K.	50

4.8	Slow and fast time constants at 300K.	51
4.9	Time constants extracted from the 77 K luminescent transients.	58
4.10	Decay time of the inhomogeneously broadened exciton DOS.	59
A.1	Geometry for the calculation of the phasematching angle	67

Acknowledgements

I would like to sincerely thank my supervisor, Dr. Jeff Young, for his extensive guidance and support in this project. It was both an honour and a pleasure to learn under the tutelage of such an amazing physicist.

I am indebted to Andras Pattantyus-Abraham, a PhD student with Dr. Michael Wolf in the Chemistry Department at U.B.C., for preparation of the samples and many fruitful discussions. I also thank him for the description of the sample preparation included in Chapter 3.

I would also like to thank my labmates, all of whom contribute to a great dynamic in the lab. In particular, I am grateful to Alex Busch for patiently helping me with the procedures for the cryostat and the optical system.

Finally, special thanks are due to my parents for their constant incredible support.

Chapter 1

Introduction

Conjugated polymers such as poly(*p*-phenylenevinylene) (PPV) have been the subject of intense study in the last decade due to their semiconductor-like properties. Their visible band-gaps and ease of production make them attractive for use in electroluminescent devices, while the quest to understand the nature of electronic excitations in these materials has fuelled the research from a fundamental standpoint.

The chemical structure of PPV is shown in Figure 1.1. The average chain length

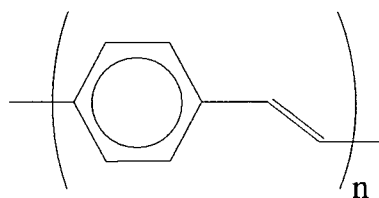


Figure 1.1: Chemical structure of PPV

in PPV consists of about 50,000 repeat units of this structure. The semiconducting properties of PPV arise because of delocalization of the π electrons in the double bonds

of both the vinylene (C=C) and phenyl units (C₆H₄). The electrons are delocalized over the effective conjugation length, which refers to a segment of the polymer chain which is unbroken by defects such as twists, bends, or impurities. The effective conjugation length determines the energies of the ground and excited states, and thus the emission energies [1]. In PPV films, the average effective conjugation length is typically about 10 repeat units [2].

Much of the early work on PPV was devoted to resolving the issue of whether the photoexcitations are best described by a semiconductor band model or a molecular approach. In the semiconductor model, the polymer is viewed as an infinite 1D one-electron system with strong electron-phonon coupling, but Coulombic forces and electron-electron correlations are ignored [3]. More recently, the evidence has pointed toward the molecular approach as being the more accurate one. Because of the significant disorder present in the PPV chains, there is a distribution of conjugation lengths and excitation energies. In the molecular picture, the excitations are Coulombically bound electron-hole pairs, called excitons, and inhomogeneous broadening of the transitions leads to the broad line shapes seen in the absorption and emission spectra.

Thus far the quantum efficiency of photoluminescence (PL) from PPV has remained relatively poor, a major obstacle for ultimate applications in electroluminescent devices. There has been considerable debate concerning the value [4]-[6], with estimates as low as 10% [4] and 20% [5]. Related materials such as MEH-PPV (poly[2-methoxy,5-(2'-ethyl-hexyloxy)-*p*-phenylenevinylene]) have been investigated, but its photoluminescence

efficiency has been found to be lower than that of PPV [7].

Interchain interactions in conjugated polymers may be partly responsible for the non-radiative quenching of excitons [5]. Interchain interactions would be reduced if individual polymer chains were isolated. An exciting development on this front has been the incorporation of PPV in a mesoporous silica host [8], [9]. Not only does this isolate chains from one another, but it opens the path to controlling the optical properties of luminescent polymers in the same manner as nanostructured semiconducting materials are tailored for specific opto-electronic purposes [10].

Time resolved photoluminescence studies have proven to be the most effective means of probing the sub-picosecond dynamics in PPV and other conjugated polymers. This thesis describes our investigation of the dynamics of excitations in PPV through the use of the photoluminescence upconversion technique [11]. The photoluminescence signal and a femtosecond laser pulse are focussed onto a suitably oriented nonlinear crystal to generate sum frequency radiation. The sum frequency signal is only generated during the time that the two beams coincide in the crystal. Therefore, by varying the delay of the gate pulse with respect to the PL, the evolution of the PL can be mapped out with a time resolution on the order of the laser pulsewidth.

We find that our 77 K luminescence transients are well fitted by bi- or tri-exponential fits. The time constants extracted from the fits are associated with a zero, one, or two-phonon sampling of a single inhomogeneously broadened exciton density of states (DOS). Data acquired at 300 K indicate a greater temperature dependence of the exciton decay

rate in the vicinity of the peak of the DOS compared to higher energies. From the 77 K data, we make a quantitative determination of the exciton decay rate from 7 meV below the peak in the DOS to an energy 330 meV higher. Over this range, and towards higher energies, the decay time varies from about 116 ps to less than 300 fs, the time resolution of our system.

The thesis is organized in the following manner. In Chapter 2, the theory governing the upconversion method is described in detail. The experimental methods used to acquire the time resolved photoluminescence data are described in Chapter 3, and the results are presented and discussed in Chapter 4. In Chapter 5 the work is summarized and some future considerations are outlined.

Chapter 2

Theory

2.1 Introduction

This experiment uses a nonlinear optical technique to time resolve the photoluminescence signal from an organic polymer. The nonlinear optical processes involved, namely second harmonic generation and sum frequency generation, are well established (see for example [12], [13]). Both processes depend on a nonlinear polarization induced in a crystal that is proportional to the second order of the electric field. This nonlinear interaction requires an intense electric field, usually produced by a laser beam. In the case of second harmonic generation, there is only one incident beam involved and the nonlinear polarization, $P^{(2)}(2\omega)$, is proportional to the square of the electric field,

$$P^{(2)}(2\omega) = \chi^{(2)} E^2(\omega). \quad (2.1)$$

The constant of proportionality, $\chi^{(2)}$, is called the second-order nonlinear susceptibility.

Sum frequency generation is a two beam mixing process in a nonlinear crystal which

produces light with a frequency given by the sum of the two incident beam frequencies. In this case, the nonlinear polarization is proportional to the product of the electric fields of the incident beams inside the crystal,

$$P^{(2)}(\omega_1 + \omega_2) = \chi^{(2)} E_1(\omega_1) E_2(\omega_2). \quad (2.2)$$

The process of sum frequency generation provides a highly effective means to time resolve, or *upconvert*, optical signals such as photoluminescence (PL). A PL beam of frequency ω_{pl} that temporally and spatially overlaps a laser pulse of frequency ω_g inside an appropriately oriented nonlinear crystal will generate a sum frequency signal at $\omega_g + \omega_{pl}$. If the laser pulse is much shorter than the time scale over which the PL is emitted from the sample, then by varying the delay time at which the laser pulse arrives at the crystal, one can map out the time evolution of the PL. In this way, the laser pulse acts as a light gate, and is termed the gate pulse, because only when the pulse is present in the crystal will a sum frequency signal be generated. This process is illustrated schematically in Figure 2.1. With the advent of mode-locked lasers producing pulses on a femtosecond time scale, sum frequency generation has become the most effective technique for obtaining sub-picosecond time resolution in ultrafast emission spectroscopy.

The most complete reference devoted to the topic of upconversion was written by Jagdeep Shah [11], one of the pioneers of the technique. Many of the following theoretical considerations were developed based on this paper and references contained therein.

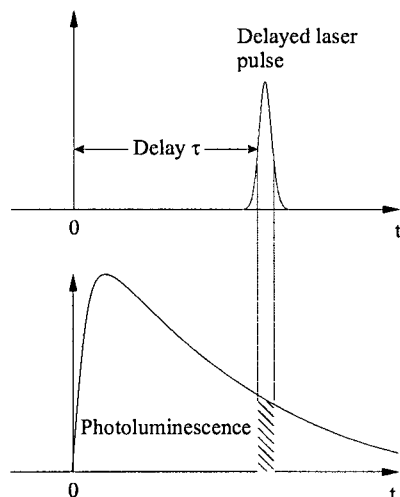


Figure 2.1: Time resolved luminescence spectroscopy.

2.2 Second Harmonic Generation

Before discussing the more complicated issue of sum frequency generation, it is worthwhile to introduce the physics behind second harmonic generation, both because it is an integral part of the experiment and because it utilizes the same concepts as its three beam partner process.

The theory¹ starts from Maxwell's equations in a form which separates the polarization, P , into linear and nonlinear terms,

$$\vec{P} = \epsilon_0 \chi_L \vec{E} + \vec{P}_{NL}, \quad (2.3)$$

where χ_L is the linear susceptibility and \vec{P}_{NL} is the nonlinear polarization. The equations

¹For a complete derivation, see [12] or [13].

can be manipulated to derive a nonlinear wave-equation,

$$\vec{\nabla}^2 \vec{E} = \mu_0 \sigma \frac{\partial \vec{E}}{\partial t} + \mu_0 \epsilon \frac{\partial^2 \vec{E}}{\partial t^2} + \mu_0 \frac{\partial^2}{\partial t^2} \vec{P}_{NL}, \quad (2.4)$$

where σ is the conductivity, ϵ is the dielectric permittivity, and μ_0 is the magnetic permeability of free space.

By limiting the problem to one dimension and considering the interaction of three waves with frequencies related by $\omega_1 + \omega_2 = \omega_3$, a set of coupled differential equations for the electric fields can be derived. Second harmonic generation is a special case of this problem where $\omega_1 = \omega_2$ and $\omega_3 = 2\omega_1$.

The issue of interest for this thesis is the efficiency of the nonlinear process. This topic will be covered in more detail in Section 2.5, but for the present purpose it suffices to quote the well-known result for the quantum efficiency of second harmonic generation within a nonlinear medium:

$$\eta_{SHG} = \frac{W_{2\omega}}{W_\omega} = 2 \left(\frac{\mu}{\epsilon_0} \right)^{3/2} \frac{\omega^2 d_{ijk}^2 L^2}{n^3} \frac{\sin^2(\Delta k L / 2)}{(\Delta k L / 2)^2} \frac{W_\omega}{A}, \quad (2.5)$$

where W_ω and $W_{2\omega}$ are the powers of the incident and generated beams, respectively; μ is the magnetic permeability of the material; ϵ_0 is the permittivity of free space; d_{ijk} is the nonlinear coefficient of the medium; L and A refer to the length and excitation area of the medium, respectively; n is the index of refraction; and

$$\Delta k = k^{(2\omega)} - 2k^{(\omega)} \quad (2.6)$$

is the phase mismatch between the wavevectors of the incident, $k^{(\omega)}$, and generated, $k^{(2\omega)}$,

beams. From this equation, it is clear that if there is not perfect phasematching - that is, Δk is not zero - then the quantum efficiency decreases with increasing Δk as

$$\eta_q(\Delta k) = \eta_q(0) \frac{\sin^2(\Delta k L/2)}{(\Delta k L/2)^2}, \quad (2.7)$$

where $\eta_q(0)$ includes the other terms from equation (2.5).

Since

$$k = \frac{n\omega}{c}, \quad (2.8)$$

the phasematching condition (eq. 2.6) is equivalent to writing

$$n^{(2\omega)} = n^{(\omega)}. \quad (2.9)$$

For most transparent materials, the index of refraction increases with increasing frequency in the visible part of the spectrum, rendering the index matching condition impossible to achieve. However, the birefringence of noncentrosymmetric crystals can be exploited to compensate for dispersion and satisfy eq. 2.9. Consequently, the second harmonic beam must be generated with an orthogonal polarization to that of the incident laser beam.

For a beam which propagates with the so-called *ordinary* polarization, the index of refraction, n_o , is *independent* of propagation direction in the crystal and is represented by a circle in the k-space diagram of Figure 2.2. However, for a beam with the *extraordinary* polarization, the index of refraction, $n_e(\theta)$, depends on the angle between the direction of propagation and the crystal symmetry direction called the optic axis (see Figure 2.3).

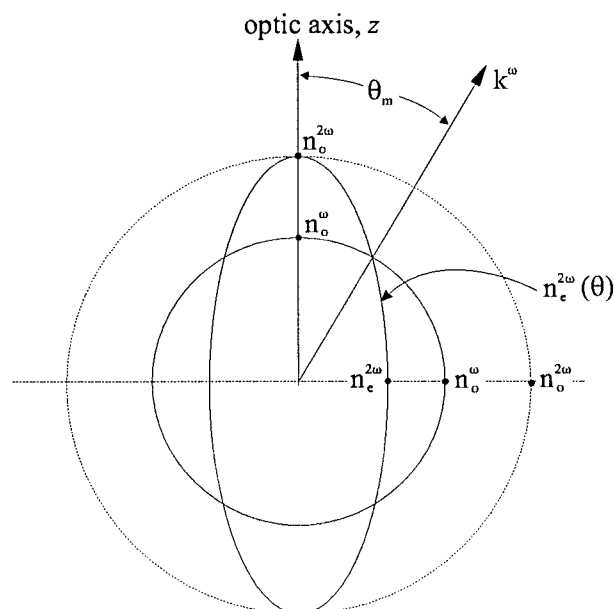


Figure 2.2: Index surfaces for the ordinary and extraordinary rays, showing $n_e^{2\omega}(\theta) = n_o^\omega$ at $\theta = \theta_m$.

The extraordinary index is given by the relation

$$\frac{1}{n_e^2(\theta)} = \frac{\cos^2\theta}{n_o^2} + \frac{\sin^2\theta}{n_e^2}, \quad (2.10)$$

which represents an ellipse with semi-major axis of length n_o and semi-minor axis of length n_e . The crystal used in this experiment was negative uniaxial, meaning $n_e(\theta) \leq n_o$ for all θ .

Figure 2.2 provides a convenient construction to determine the phasematching angle, θ_m . We can see that if $n_e^{2\omega} < n_o^\omega$, then there must be an intersection between the n_o^ω circle and the $n_e^{2\omega}(\theta)$ ellipse. Therefore, an ordinary beam of frequency ω that is launched at an angle θ_m to the optic axis will generate an extraordinary beam of frequency 2ω

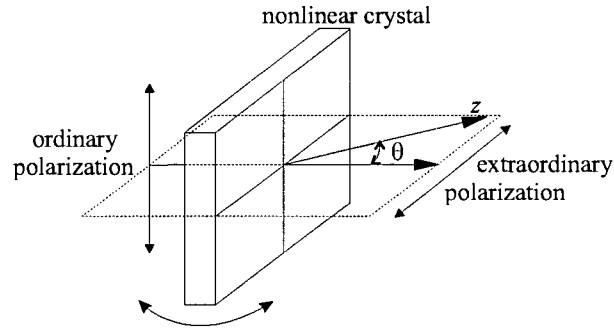


Figure 2.3: Light propagation at an angle θ to the optic axis, z , of a nonlinear crystal. Phasematching is achieved by rotating the crystal so that $\theta = \theta_m$.

along the same direction.

Substituting $n_o^\omega = n_e^{2\omega}(\theta_m)$ into equation (2.10) yields

$$\frac{1}{(n_o^\omega)^2} = \frac{\cos^2 \theta_m}{(n_o^{2\omega})^2} + \frac{\sin^2 \theta_m}{(n_e^{2\omega})^2}, \quad (2.11)$$

which can be solved analytically for θ_m to give

$$\sin^2 \theta_m = \frac{(n_o^\omega)^{-2} - (n_o^{2\omega})^{-2}}{(n_e^{2\omega})^{-2} - (n_o^{2\omega})^{-2}}. \quad (2.12)$$

2.3 Sum Frequency Generation

The frequency mixing technique of sum frequency generation used in this experiment is based on the same principles as second harmonic generation. However, it consists of a three beam interaction in a non-collinear geometry as opposed to the two beam (collinear) SHG process treated in the previous section.

This section details how the crystal angle is chosen to phasematch the upconversion process. This is a relatively straightforward but extremely important calculation, because without prior knowledge of where to position the crystal it is difficult to generate an upconverted signal.

To satisfy energy conservation, we have

$$\omega_{pl} + \omega_g = \omega_s, \quad (2.13)$$

where the subscript pl refers to the photoluminescence, g refers to the gate pulse from the laser, and s refers to the sum frequency light.

Similar to second harmonic generation, efficient sum frequency generation requires phase matching between the two incident beams and the sum frequency signal. This is simply conservation of momentum, with the sum of the two incident wave vectors equaling the resultant sum frequency wave vector for phase matched generation:

$$\vec{k}_{pl} + \vec{k}_g = \vec{k}_s. \quad (2.14)$$

The sum frequency process must consist of a combination of extraordinary (E) and ordinary (O) rays. However, for negative uniaxial crystals, it can be shown that the sum frequency ray must be an E ray [11]. That leaves two possible processes: $O + O \rightarrow E$ (type I) and $O + E \rightarrow E$ (type II). This experiment utilizes only type I phasematching.

The calculation of the appropriate crystal angle proceeds as follows. For type I phasematching, both the gate and PL beams are polarized as O rays. Therefore, their indices are simply determined from the empirical dispersion relations, which can be looked

up in the Handbook of Nonlinear Optical Crystals [14]. Provided the angle between \vec{k}_{pl} and \vec{k}_g inside the crystal is known, this information completely determines the incident wave vectors, and hence by eq. 2.14 gives \vec{k}_s . The sum frequency, ν_s , is trivially found from equation 2.13. Knowing the k-vector magnitude and frequency, one can solve eq. 2.8 for the sum frequency index, $n_s(\theta_m)$.

Having found $n_s(\theta_m)$, one can solve eq. 2.10 for θ_m in the same manner as eq. 2.12, with the label 2ω replaced by s to indicate the sum frequency ray:

$$\sin^2(\theta_m) = \frac{(n_s(\theta_m))^{-2} - (n_o^s)^{-2}}{(n_e^s)^{-2} - (n_o^s)^{-2}}, \quad (2.15)$$

where the notation n_e^s refers to the extraordinary index at the sum frequency.

The calculation is complicated by the fact that one can only measure the angle between the PL and gate beams external to the crystal. The internal angle is determined by refraction at the interface according to Snell's law. However, one cannot know the angle of incidence of either of these beams exactly, because it changes as the crystal is rotated to the proper phasematching angle. In essence, the calculation of the crystal angle requires as one of its input parameters the very same crystal angle. A short Maple code using an iterative numerical routine was written to calculate the proper angle (see Appendix 1).

2.4 Angle of Acceptance

A schematic of the laser excitation of the sample and the subsequent emission of photoluminescence is shown in Figure 2.4. When the PL is focussed onto the crystal it spans a certain solid angle, $\Delta\phi_f$, determined by the collection optics. There is a limit to this solid angle, called the angle of acceptance ($\Delta\phi_{acc}$), beyond which there will be no sum frequency photons generated.

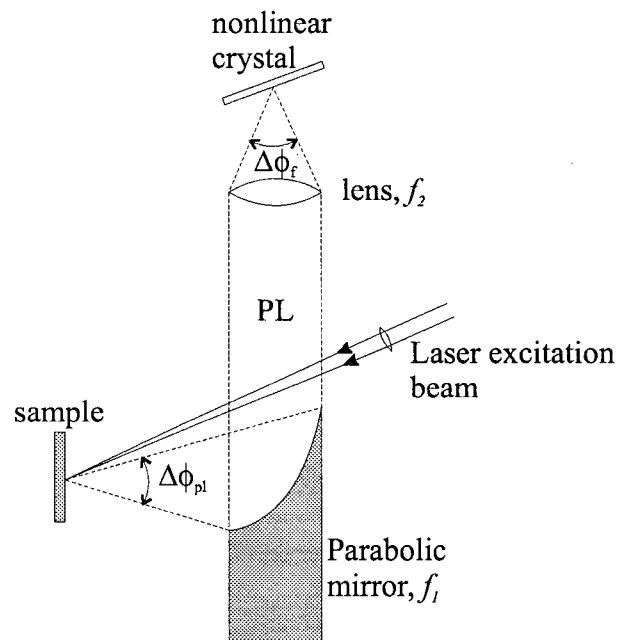


Figure 2.4: Excitation and collection of photoluminescence. A solid angle $\Delta\phi_{pl}$ of PL is collected by a parabolic mirror (f_1) and focussed by a lens (f_2) at a solid angle of $\Delta\phi_f$.

To calculate the angle of acceptance [15], we need to calculate the solid angle which corresponds to a given phase mismatch, Δk . The non-collinear geometry is detailed in

Figures 2.5 and 2.6. The gate beam is defined by \vec{k}_g , whereas the range of PL wave vectors for a given ω_{pl} is indicated by the locus of \vec{k}_{pl} . The locus of \vec{k}_s is an ellipse since it is polarized as an extraordinary ray. However, we shall approximate it as circular, which is well justified considering that in the frequency range of interest, the values of n_o and n_e (the semi-axes of the ellipse) are less than 8% apart. The phase mismatch is indicated by Δk .

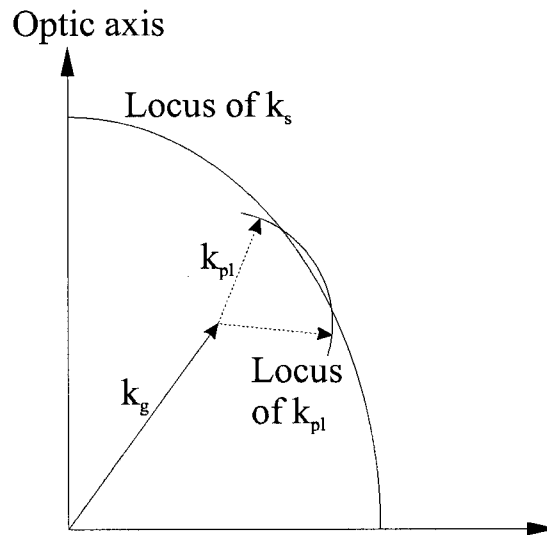


Figure 2.5: Phase matching detail for the sum frequency generation process $\vec{k}_g + \vec{k}_{pl} = \vec{k}_s$.

We use the cosine law to find an expression for the half-angle, θ (Figure 2.6):

$$k_s^2 = k_g^2 + (k_{pl} + \Delta k)^2 + 2k_g(k_{pl} + \Delta k) \cos \theta. \quad (2.16)$$

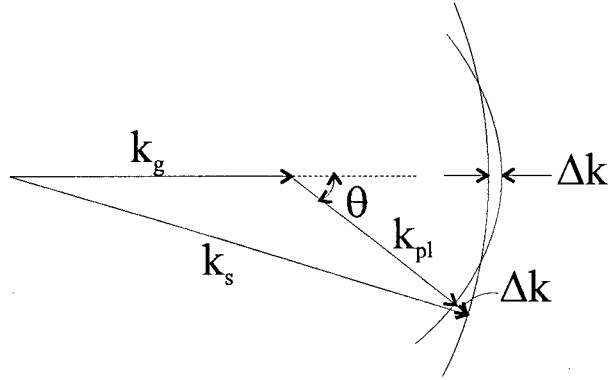


Figure 2.6: Half-angle of acceptance, θ , determined by the phase mismatch, Δk .

Substituting

$$k_s = k_g + k_{pl} - \Delta k \quad (2.17)$$

and neglecting terms that are second order in Δk yields

$$k_g k_{pl} - \Delta k (k_g + 2k_{pl}) = k_g (k_{pl} + \Delta k) \cos \theta. \quad (2.18)$$

We then substitute the small angle approximation $\cos \theta = 1 - \theta^2/2$ and rearrange terms to get

$$\theta^2 = \frac{4\Delta k (k_{pl} + k_g)}{k_g k_{pl} + k_g \Delta k}. \quad (2.19)$$

At this point, the Δk term in the denominator can be neglected, and we can substitute $k_s \approx k_g + k_{pl}$ in the numerator. Collecting terms and rearranging leads to a half-angle of

$$\theta = \sqrt{\frac{4\Delta k}{k_{pl}(1 - k_{pl}/k_s)}}. \quad (2.20)$$

The half-angle of acceptance, θ , is defined to be the angle at which the quantum efficiency of upconversion (eq. 2.5) is reduced by half from its maximum value. Because $\sin^2(x)/x^2 = 0.5$ when $x = \pm 1.39$, this condition corresponds to a phase mismatch $\Delta k = 2.78/L$.

The solid angle external to the crystal is given by

$$\Delta\phi_{acc} = \pi(\theta n_{pl})^2. \quad (2.21)$$

Making the substitution for Δk and $k = 2\pi n/\lambda$ in equation (2.20) leads to the final result,

$$\Delta\phi_{acc} = \frac{5.56 n_o^{pl} \lambda_{pl}}{l(1 - n_o^{pl} \lambda_s / n_s \lambda_{pl})}. \quad (2.22)$$

2.5 Upconversion efficiency

We shall follow Shah's analysis on how to maximize the upconversion efficiency. It can be shown, starting from the coupled equations derived from Maxwell's equations, that under the condition of negligible gate beam depletion, the quantum efficiency for sum frequency generation for a phase matched collinear geometry is given by

$$\eta_q(0) = \frac{2\pi^2 d_{eff}^2 L^2 (P_g/A)}{c\epsilon_o^3 \lambda_{pl} \lambda_s n_o^{pl} n_o^g n_s (\theta_m)}, \quad (2.23)$$

where d_{eff} is the effective nonlinear coefficient of the crystal, P_g is the power of the gate beam, A is the area of the gate beam at the nonlinear crystal, and c is the speed of light. Although the present experiment uses a more complex noncollinear geometry with

angular spreading of the beams, we use this expression for illustrative purposes in the following treatment.

Our goal is to find the appropriate focal lengths, f_1 and f_2 , for the two lenses which collimate and focus the PL onto the nonlinear crystal. More specifically, we are interested in the magnification, $M = f_2/f_1$, required to optimize the upconversion. As will be shown below, there are two competing parameters: the area of the PL spot at the crystal, A_X , and the solid angle of convergence of the focussed PL, $\Delta\phi_f$. The ideal situation is to have a tightly focussed PL spot that does not exceed the crystal's acceptance angle. We first need to find how these quantities are related to the focussing lens. The Rayleigh diffraction limited spot radius, q , of a collimated beam of diameter d and wavelength λ focussed by a lens of focal length, f , is given by

$$q = 1.22 \lambda f/d. \quad (2.24)$$

The solid angle, $\Delta\phi_f$, is given by

$$\Delta\phi_f = \pi d^2/4f^2. \quad (2.25)$$

Therefore, since $A_X = \pi q^2$, $A_X \propto f^2$ whereas $\Delta\phi_f \propto 1/f^2$. Consequently, shortening the focal length will decrease the spot size at the expense of increasing the solid angle.

Suppose the sample is excited over a spot of size A_s . A solid angle $\Delta\phi_{pl}$ of PL is collected by a lens of focal length f_1 and focussed onto the crystal with a lens of focal length f_2 . The spot-size at the crystal is given by

$$A_X = M^2 A_s. \quad (2.26)$$

The solid angle of convergence of the PL focussed to the crystal is given by

$$\Delta\phi_f = \Delta\phi_{pl}/M^2. \quad (2.27)$$

The gate beam, which has peak power P_g , is focussed to a spot of size A at the nonlinear crystal, which has quantum efficiency $\eta_q(0)$ as given by equation 2.23. For this experiment the waist of the collimated gate beam is small enough that it is focussed well within the acceptance angle of the crystal. Assuming the sample emits N_{pl} photons of PL per steradian per unit time in the energy range of interest, and that N_s upconverted photons are generated at the nonlinear crystal per unit time, we can write

$$N_s = N_{pl} \Delta\phi_{pl} \eta_q(0) \left(\frac{A}{A_x} \right)_{\leq 1} \left(\frac{\Delta\phi_{acc}}{\Delta\phi_f} \right)_{\leq 1}, \quad (2.28)$$

where $\Delta\phi_{acc}$ is the acceptance angle of the crystal as defined by equation 2.22. The two factors in parentheses indicate that the upconversion efficiency will be reduced if either the PL spot-size at the crystal exceeds the gate spot-size at the crystal or the solid angle of convergence exceeds the acceptance angle of the crystal. Neither of these factors can exceed 1, however, since the best that can be done is to upconvert with efficiency $\eta_q(0)$ all the PL photons, N_{pl} , that are collected in a solid angle $\Delta\phi_{pl}$.

To bring the magnification, M , into the picture, we can rewrite eq. (2.28) with the help of (2.26) and (2.27) to give

$$N_s = N_{pl} \Delta\phi_{pl} \eta_q(0) \left(\frac{A}{A_s M^2} \right)_{\leq 1} \left(\frac{\Delta\phi_{acc}}{\Delta\phi_{pl}/M^2} \right)_{\leq 1}. \quad (2.29)$$

Finally, we let

$$M_1^2 = \Delta\phi_{pl}/\Delta\phi_{acc} \quad (2.30)$$

and

$$M_2^2 = A/A_s, \quad (2.31)$$

so that eq. 2.29 becomes

$$N_s = N_{pl} \Delta\phi_{pl} \eta_q(0) \left(\frac{M_2^2}{M^2} \right)_{\leq 1} \left(\frac{M^2}{M_1^2} \right)_{\leq 1}. \quad (2.32)$$

Let us first consider the case of $M_1 > M_2$. In this scenario, the upconversion efficiency is optimized when $M_2 < M < M_1$, so that $N_s \propto M_2^2/M_1^2$. To explain why M should be bounded in this manner, consider what happens when $M < M_2$. The factor M_2^2/M^2 cuts off at a value of 1 (because we can make no gains by having the PL spot smaller in area than the gate spot) and we are left with $N_s \propto M^2/M_1^2$. But $M < M_2$, so clearly we are worse off. A similar argument can be made to prove that M should not exceed M_1 . In short, N_s will drop off as $1/M^2$ if M is not between M_2 and M_1 .

If, however, $M_2 > M_1$, equation 2.32 must be modified slightly, because otherwise the factors in parantheses exceed 1, which, as explained earlier, is unphysical. The modified equation now reads

$$N_s = N_{pl} \Delta\phi_{pl} \eta_q(0) \left(\frac{M_2^2}{M^2} \right)_{\leq 1} \left(\frac{M^2}{M_1^2} \right)_{\leq 1} \left(\frac{M_1^2}{M_2^2} \right). \quad (2.33)$$

Once again the best choice for M is such that $M_1 < M < M_2$, or the efficiency will fall off as $1/M^2$.

With the efficiency defined as

$$\eta = N_s/N_{pl}, \quad (2.34)$$

the maximum upconverted efficiency, η_{\max} , can now be found by substituting $\eta_q(0)$ from eq. 2.23 into eq. 2.32 and simplifying to give

$$\eta_{\max} = \beta_{\max} P_g \quad M_1 > M_2 \quad (2.35)$$

$$\eta_{\max} = \beta_{\max} P_g (M_1/M_2)^2 \quad M_1 < M_2 \quad (2.36)$$

where

$$\beta_{\max} = \eta_o(\Delta\phi_{acc})(L^2/A_s) \quad (2.37)$$

and

$$\eta_o = \frac{2\pi^2 d_{\text{eff}}^2}{c\epsilon_o^3 \lambda_{pl} \lambda_s n_o^{pl} n_o^g n_s(\theta_m)}. \quad (2.38)$$

In light of these considerations, the focal lengths f_1 and f_2 should be chosen such that $M_2 < M < M_1$ in order to optimize the upconverted signal.

Chapter 3

Experiment

To reflect the large amount of work required to take the experiment from beginning to fruition, this section will discuss the optical alignment in considerable detail.

3.1 System Overview

The laser is a Spectra-Physics mode-locked Titanium:Sapphire laser pumped by an Argon ion laser. It is tunable over a wavelength range of 735-820 nm, with a power of 800 mW at 800 nm. When properly mode-locked, the laser emits ~ 100 femtosecond transform-limited pulses with a $\text{sech}^2(t)$ temporal profile at a repetition rate of 82 MHz.

The laser and optics are mounted on an air-suspension optical table. The samples under investigation are housed in a cryostat which was kept under liquid Nitrogen cooling at 77 K for the majority of the data collection. A heater controlled by a Lakeshore temperature controller allows control of the sample temperature to within 0.1 K.

The optical elements are arranged as shown in Figure 3.1. The beam is split at B/S

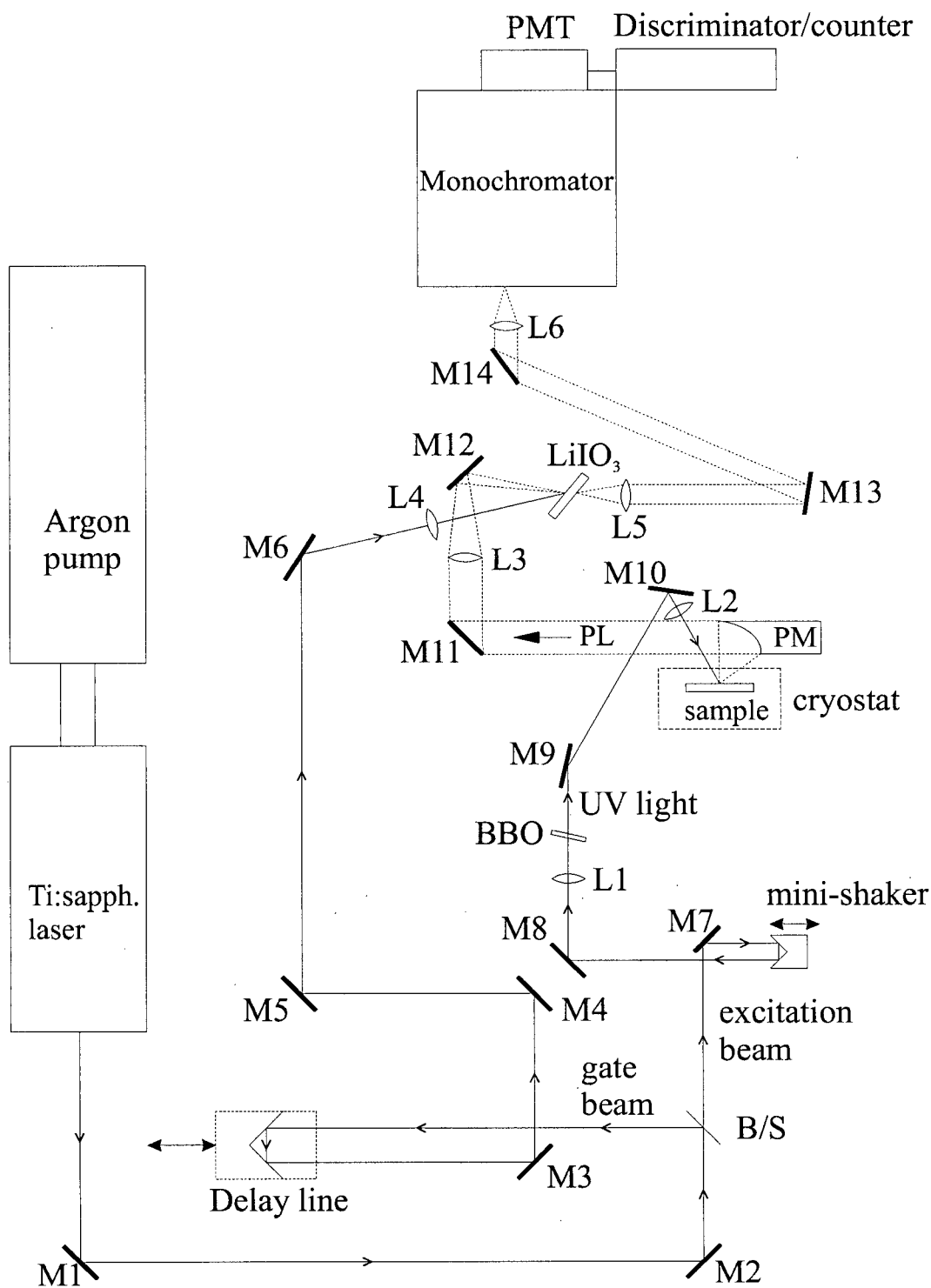


Figure 3.1: Experimental set-up for femtosecond time resolved photoluminescence spectroscopy.

into the gate and excitation beams. The gate beam first hits a gold-plated¹ retro-reflector mounted on a linear translation stage. The retro-reflector, or corner cube, is composed of three mirrors and serves to reflect the beam in the same direction from which it came, but laterally displaced by about 1 cm.

After hitting the retro-reflector, the beam hits a series of mirrors designed to match the path length of the excitation beam and guide the gate pulse down to the crystal. After the final turning mirror, M6, the pulse is focussed onto the nonlinear crystal by a 10 cm lens (L4) mounted on a translation stage. The translation stage allows control of the spot-size at the crystal, an important parameter for upconversion experiments. The lens is aligned to focus the beam at the centre of the rotation stage, which ensures the beam doesn't walk when the crystal is rotated². Because of the relatively narrow bandwidth of the laser (about 15 nm when mode-locked), chromatic aberration in the gate-focussing lens is negligible, but introduces dispersion which slightly clouds the precise determination of zero delay time.

The nonlinear element is a 1 cm x 1 cm x 0.5 mm crystal composed of Lithium Iodate (LiIO_3) cut at an angle of 44.51° to the optic axis. With such an angle, the crystal was designed to allow normal incidence second harmonic generation from 800 nm laser pulses. While perfectly adequate for the sample investigated in this experiment, the angle is not ideal because the rotation necessary for phasematching almost occludes the

¹Gold is an excellent infrared reflector.

²Practically, this is difficult to avoid.

beam with the housing of the crystal. The 0.5 mm thickness is comparable to that used in the literature, and balances the competing criteria of upconversion efficiency and time resolution. The crystal is mounted on a translation stage running parallel to the surface of the crystal, which in turn sits upon a motor-driven rotation stage with 0.1° accuracy. Below the rotation stage sits another translation stage allowing the crystal to be moved through the focus of the beam.

After being split from the gate beam, the excitation beam hits a retro-reflector mounted on a mini-shaker, the purpose of which will be described below, and is then directed towards the cryostat by a turning mirror (M8). Two turning mirrors (M9 and M10) direct the beam behind the cryostat, and a 10 cm lens (L2) focusses the beam onto the sample in the cryostat. For the PPV polymer, the excitation must be in the UV, and so a 5cm focal length lens (L1) and a thick (1 mm) BBO (Beta-Barium Borate) crystal are inserted into the beam path to generate the second harmonic of the infrared laser. The UV beam diverges from the BBO crystal until it hits lens L2.

The photoluminescence is collimated by a 90° parabolic mirror (PM) of focal length $f = 57.5$ cm and focussed onto the crystal by a 15 cm lens (L3)/turning mirror (M12) combination. A short focal length (7.5 cm) UV lens (L5) is used to collimate light from the crystal. Two 2 inch UV-coated mirrors direct the light into a 10 cm UV lens (L6) which is focussed to the input slit of the monochromator. The photon counting detection is achieved with a photomultiplier tube (PMT) connected to a computer monitored counter. LabView programs allow computer control of the monochromator (MonoRead.vi

and MonoWrite.vi), crystal rotation (Rotate.vi), PMT counts (Select Detector & Take Measurement.vi), and acquisition of spectra (ScanAndSave.vi).

Ideally, all of the focussing elements would be reflective optics in order to eliminate chromatic aberration, which causes the focal length to depend on the wavelength of light. The dispersive lenses used in the present set-up require slight adjustments when varying the wavelength of PL being monitored. This did not turn out to be a major problem, and the refractive elements do have the advantage of being much easier to align in the first place.

3.2 Photon counting and data acquisition

Because of the low light levels typical of upconversion experiments, a photon counting technique was used to detect the upconverted signals. In the present set-up, an Electron Tubes 9784A PMT with peak spectral response from 250-350 nm is mounted in a light-tight housing after the monochromator. A discriminator converts the signal pulses to a TTL signal which is monitored by a counter on a PC board. The discriminator level and PMT voltage (800 V) were selected to optimize signal to noise. Because the counting system is very sensitive to electrical noise, the BNC cables connecting the PMT/discriminator/counter were shielded with a layer of aluminum foil. Care was taken to minimize any stray light impinging on the PMT.

The dark counts of the PMT double every 5 degrees the room temperature increases,

making the PMT very sensitive to changes in room temperature. Considerable effort was taken to try to prevent the room temperature from increasing during the day, including covering the windows (which are shielded by light-tight blinds) in Al-foil to reflect the sunlight. The PMT also warms up internally, a process which increases the noise over the course of a day. A cooling system to negate this effect is planned for the future.

3.3 Alignment

3.3.1 General

In principle, the sample can be excited in either a transmission or reflection geometry. For PPV, which has a relatively broad PL spectrum, there is considerable reabsorption of the high energy PL components in transmission, and so a reflection geometry was adopted.

The two set-ups are not trivially interchangeable. Originally designed to upconvert GaAs quantum well PL in a transmission geometry, the excitation beam lengthened by about 40 cm during conversion to the reflection geometry, which is beyond the limits of the translation stage controlling the delay. To compensate, the gate path length was lengthened an equivalent amount by moving the two mirrors M3 and M4.

In its present configuration, the translation stage must be controlled by hand. One rule of thumb to ensure repeatability and consistency of results is to account for backlash effects by always approaching a given delay in the same direction (e.g. increasing delay).

Careful alignment of the translation stage is required so that the reflected beam position stays fixed when the delay is varied. It is crucial that the gate beam after M3 be aligned parallel to the axis of the translation stage. If it is not, the reflected beam will walk depending on the stage position. The alignment can be accomplished by fixing an aperture in front of the retro-reflector and ensuring the beam passes through the aperture at both the near and far limits of motion. With the beam parallel to the axis of motion, the retro-reflector is guaranteed to reflect the beam in the same direction independent of position.

3.3.2 Acceptance angle considerations

The acceptance angle of the LiIO_3 crystal is found from equation 2.22 to be 0.0286 steradian. Assuming

$$\Delta\phi_{acc} = \pi(\Delta\theta)^2, \quad (3.1)$$

this solid angle corresponds to a half-angle, $\Delta\theta$, of 5.5° . This was calculated with a PL wavelength (for PPV at 77 K) of 530 nm, $n_o^{pl} = 1.898$, $\lambda_s = 319$ nm, and $n_s(\theta_m) = 1.887$.³ The radius of L3 is 12 mm, so an appropriate focal length lens to fill the acceptance angle is

$$f = 12/\tan(5.5), \quad (3.2)$$

³ $n_s(\theta_m)$ was determined using the Maple code, but is within 1% of the collinear value, which is trivially found using the phase matching condition $n_s(\theta_m) = n_o^{pl} \frac{\lambda_s}{\lambda_{pl}} + n_o^g \frac{\lambda_s}{\lambda_g}$.

or 125 mm. A 150 mm focal length lens was chosen to satisfy this criterion and the physical constraints on the optical table.

3.3.3 Imaging

A Panasonic CCD camera is used to image the nonlinear crystal plane. The gate and PL spots are only a few hundred microns in diameter, but they must be overlapped and matched in size in order to generate an upconverted signal. A thin strip of teflon is placed directly on the crystal surface and the sample is then translated to align the beams on the teflon, which yields much more scattered light than the crystal. The camera is unable to see the PL on the crystal, but easily resolves the spot scattered off the teflon. In order to resolve the true spot-size, the beam should be sufficiently attenuated to avoid saturation of the camera.

It is important to ensure that the translation stage runs parallel to the surface of the crystal, so that when the crystal is translated the plane of overlap of the PL and gate beams remains within the crystal. In fact, one must still compensate for the fact that the teflon lies on the front surface of the crystal, whereas optimum overlap between the PL and the gate must occur at the middle of the crystal, which is 250 microns behind the tape. This compensation is not difficult, and once an upconverted signal has been found it requires optimization no matter how carefully the spots are aligned using the camera.

3.3.4 Laser upconversion

The point of zero delay between the excitation and gate beam paths refers to the position where a pulse which reflects off the surface of the sample will reach the upconversion crystal at the same time as the gate pulse. If the crystal is oriented properly, sum frequency generation is generated at twice the laser frequency and is easily visible to the naked eye.

In order to position the crystal correctly, the geometry of the two incident beams must first be established. The best way to accomplish this is to observe the second harmonic signals from each beam alone, using IR laser light scattered from the sample instead of PL, which is much too weak to produce an observable second harmonic. One difficulty is that because of chromatic aberration in L3, the scattered IR is not close to being focussed at the crystal when this lens has been aligned for PL. Therefore, the lens must be translated to compensate for this effect and focus the IR at the sample.

The gate pulse second harmonic is extremely strong because of its intensity and tight focus. Once the beam has been sufficiently attenuated with neutral density filters, a detector can be used to accurately find the crystal angle (within 0.1°) to optimize the second harmonic signal. Similarly, the second harmonic signal can be found from the sample beam. Because it is the same frequency as the gate beam, the second harmonic signal will be found at the same angle θ_m with respect to the optic axis of the crystal. To find the angle between the incident beams one then simply measures the angle the

crystal was rotated between the second harmonic of each beam.

In practice, the second harmonic of the scattered laser light from the sample is difficult to observe on a Silicon photodetector placed after the sample due to insufficient intensity and the beam area diverging to exceed the active area of the detector. The best solution is to twist the sample probe within the cryostat so that the IR beam reflects off the surface of the sample (or in some cases the glass mount over the sample) and is then collected in the same manner as the PL. This is not exact, because the beam position at the crystal is highly sensitive to the rotation of the sample probe, which is a rather coarse procedure. As a result, the reflected beam does not perfectly trace the PL path to the crystal. Nevertheless, since the reflected light is much stronger than the scattered light, its second harmonic is easily detected. The ease of this technique outweighs the slight uncertainty incurred by rotating the sample and allows measurement of the angle between the incident beams to within a degree or so.

Once the angle between the input beams is established, this can be entered into the Maple program to determine the appropriate angle for laser upconversion. With the sample still rotated and the crystal correctly positioned, the focussed sample and gate spots are overlapped on the crystal with the aid of the camera. A Si detector is then positioned close to the crystal at a point midway between the exiting laser beams. The active area is shielded by a UV bandpass filter to block stray light.

The detector is used to find the upconverted laser signal, which indicates the zero delay point of the gate beam. Since each optical arm is over 3 metres long and involves

many optical elements, it is impractical to measure these lengths to the 300 micron precision required to observe a signal.

The trick used is to employ a shaker in the excitation beam path. The shaker is an integral part of a separate four-wave mixing experiment and allows one to vary the delay between two laser pulses hitting the sample under study. For the upconversion experiment, the shaker is invaluable in alignment of the zero delay for two reasons. The first is that it increases the difference in path length over which one can observe the upconverted laser pulse from about 300 microns to more than 2 mm, or twice the amplitude of oscillation of the shaker. The second, and more important reason, is that the upconverted laser pulse can be measured as an AC signal with the shaker in operation. Without the shaker, and assuming the two beam paths are closely aligned, one must place a detector at the appropriate location after the upconversion crystal and scan the delay line translation stage very slowly while observing a DC level on an oscilloscope monitoring the detector. The slight increase in signal associated with the upconverted laser beam is easily missed. By contrast, with the shaker, one can set the scope in AC coupling mode and mechanically drive the translation stage. Again assuming that the crystal is rotated properly and the detector is located in the correct place, as the translation stage passes through the zero delay point, two spikes flash across the scope screen, one each for the forward and backward pass of the shaker through the zero delay point.

If the alignment is not quite correct or the signal is weak, the upconverted signal is

easily missed even with the shaker on. In this case, the delay line needs to be scanned by hand. In many instances an AC signal of about 1 mV was observed above a noise level of about 1 mV that would have been impossible to observe with DC coupling on the scope because of a several mV DC background due to stray laser light.

Once a hint of signal is observed, it is easily optimized. A combination of tweaking M12 and rotating the crystal usually results in a many-fold increase in the upconverted laser signal, often from a few mV to hundreds of mV. To find the zero delay exactly, the shaker is turned off and the delay line tweaked to maximize the signal on the detector.

3.3.5 Alignment of collection optics

If aligned properly, the upconverted laser pulse is easily visible by eye and becomes an invaluable alignment tool for the collection optics. The UV lens L5 is first centred on the signal and then bolted to the table. The two UV mirrors (M13 and M14) are positioned to direct the beam through the centre of L6 and focus it onto the input slit of the monochromator.

The double grating monochromator contains two sets of gratings: an IR grating with 600 grooves/mm blazed at 750 nm, and a UV grating with 1200 grooves/mm blazed at 300 nm. The UV grating diffraction efficiency is far below nominal, contradicting the specifications from the manufacturer, which indicate comparable efficiency for the IR and UV gratings at 500 nm. Empirically it was found that the UV grating is about 6 times

less efficient than the IR grating for a given 500 nm signal. Given the difficulty of finding an upconverted PL signal, we decided to bypass the second grating of the monochromator (and thus halve the grating losses) by placing a UV mirror and lens after the middle slit and directing the signal to the detector out a hole in the side of the housing.

The output signal from the monochromator is very sensitive to the incident angle of the beam. With the lid of the monochromator removed the signal can be followed through to the output hole. Significant gains can be made by adjusting the two UV mirrors iteratively to optimize the input coupling of the beam (ideally normal to the entrance slit). This alignment should be preserved with the aid of two apertures before the entrance slit. The position of the PMT also requires optimization, which can be achieved by attenuating the beam with many neutral density filters and observing the count rate as the position is adjusted.⁴

The collection optics are aligned to image source light from the crystal and focus it on the detector. It is convenient to have some other means to align the optics from day to day besides the laser upconverted signal, which requires re-positioning of the sample and crystal. Fortunately there is a very useful alternative. The gate beam is so intense that despite the crystal being rotated more than 45° from phasematching, there is a significant second harmonic background generated. This light is imaged by lens L5 in the same way as the upconverted PL because it is generated from the same point on the

⁴More than 15 million counts/second (cps) can damage the PMT, but a signal not exceeding 1 million cps suffices for alignment.

crystal. Chromatic aberration is not a problem because the upconverted PL and gate second harmonic signals are within 80 nm of each other. Experience has shown that the upconverted PL is optimized at exactly the alignment which maximizes the gate second harmonic signal, making this an ideal reference signal.

The PL signal should be maximized before attempting to upconvert it. After the point of zero delay is found, the sample is rotated back into alignment with the parabolic mirror. To allow measurement of the PL spectrum without changing any of the alignment, a kinetic-mounted mirror can be inserted in the PL beam path before M11. The collimated PL then travels down the table⁵ and is focussed into the monochromator by L6. Great care must be taken to avoid damaging the PMT with the full strength of the (time-integrated) PL signal. Either the PMT must be removed and replaced with a Si detector, which is usually undesirable if the PMT position has been carefully optimized, or several neutral density filters must be inserted to reduce the intensity of the PL. The monochromator is usually switched to the IR grating to take PL spectra, but must be set to the UV grating when measuring signals at wavelengths less than 450 nm.

Usually the monochromator is positioned at the maximum PL wavelength to optimize the signal. The PL strength is very sensitive to the excitation intensity, which is most directly controlled by varying the spot-size. Once the minimum spot-size is roughly found using the camera imaging technique, significant gains (factors of 2) can still be made by

⁵In the current set-up, the nonlinear crystal must be rotated out of the way and the camera lens mount lifted out of the beam path.

tweaking the position of the sample. The sample is mounted at the end of a 1 metre long probe inserted down the middle of the cryostat. If the top of the probe is moved slightly up or down, this varies not only the height but also the depth of the sample with respect to the focus because the probe flexes slightly on each motion. Once the PL signal strength is optimized, the kinetic mirror is then removed and the PL is imaged at the crystal.

With the geometry of the incident beams established, the Maple code (Appendix 1) is used to find the proper angle for phasematching the peak of the PL with the gate pulse. The crystal is rotated the appropriate amount and, using the CCD camera to image the crystal plane, the gate and PL spots are overlapped on the teflon tape. Optical filters are used to screen the IR and UV components of the light scattered from the PPV sample. These filters are inserted at a place where the beam is collimated (usually between M11 and L3) to avoid displacing the beam.

Ideally the gate and PL spot sizes should be related according to the considerations of Section 2.5. That is, assuming the acceptance angle constraint has been satisfied, we should choose $f_2^2/f_1^2 > A/A_s$, where the first term is the ratio of the squares of the focal lengths of L3 and the parabolic mirror (PM), and the second term is the area of the gate over the sample excitation area. However, this is not a trivial process. One complication is the blurry PL spot, due in part to chromatic aberration and in part to the shape of the UV excitation spot. The UV beam that is generated at the BBO crystal does not have a circular cross-section due to the asymmetric process of phase matching. Therefore,

the spot that is focussed onto the sample is oblong in shape, which produces PL that is hard to focus tightly at the crystal. Once L3 was chosen to satisfy the acceptance angle constraint, it was found empirically that the maximum upconverted signal was always observed when the gate was as small as possible, which was typically a factor of 2 or 3 smaller in area than the PL spot-size. A more accurate alignment is not possible without reflective optics.

The second harmonic gate background that is so useful in alignment can also be the greatest bane of the experiment. Because of the high sensitivity of the photomultiplier tube and the reduced stray light rejection of the adapted monochromator, the gate background is sufficient to completely obscure the upconverted PL signal. The laser was red-shifted to keep the gate background away from the upconverted signal, which was found between 320 and 330 nm, and typically tuned to 800 nm, which fortuitously corresponds to its maximum power output of about 800 mW. A Newport UG11 filter, which transmits about 80% of the incident intensity at 320 nm and blocks light above 400 nm⁶, was used to block the second harmonic gate background. Without this filter, the weak upconverted PL signal would be lost in the noise.

⁶There is a small 8% transmission peak centred at 720 nm.

3.4 Sample Preparation

The polymer precursor was prepared by following a literature procedure [16] with some minor deviations.⁷

3.4.1 Monomer purification

The monomer, p-xylylenebis(tetrahydrothiophenium chloride) (Aldrich), was purified by dissolution in a small amount of water followed by filtration to remove the insoluble impurities. Cold acetone was added to the filtrate and the resulting precipitate was filtered off, followed by drying under flowing nitrogen.

3.4.2 Precursor polymerization

A typical preparation is described here. A weight of 2.04 g (5.8 mmol) of monomer was dissolved in 23 mL of distilled water, degassed and cooled to 0°C in an ice bath. A 1.0 M aqueous NaOH solution was similarly degassed and cooled. An equimolar amount of NaOH was then added to the monomer solution; after 1 minute, a rapid rise in the viscosity was observed. The polymerization was stopped after 3 minutes using 1.5 M aqueous HCl and the mixture was transferred to a SPECTRA-POR dialysis membrane (molecular weight cutoff 6000 - 8000 g mol⁻¹). This was placed in a large amount of distilled water and left standing for 1 day. The colourless precursor was precipitated

⁷The sample was prepared by Andras Pattantyus-Abraham in Michael Wolf's group.

using a mixture of 5 g of NH_4Cl and 500 mL of isopropanol. The resulting solid was filtered and dried in air.

3.4.3 Thin film preparation

The polymer precursor was dissolved in 1:1 water/methanol mixture. A small amount was dropped onto a glass substrate with a pipette and left to dry in air. The substrate was then placed under vacuum and heated at 190°C for 6 hours, which resulted in a bright yellow, optically thick film.

3.5 Data collection

The time resolved data in Chapter 4 are presented as plots of intensity as a function of delay for a given PL energy. The frequency dependence of the upconversion system was not calibrated against standards, and so the upconverted spectrum at a given delay will not be discussed.

The data were collected by fixing the monochromator and varying the delay. In this mode of operation, the relative coupling efficiencies of different PL energies at the non-linear crystal and monochromator entrance slit become irrelevant because the coupling is fixed.

After finding an upconverted signal, it is optimized by tweaking mirror M12. The gate beam is not adjusted because it serves as the reference used to align the collection optics.

Small adjustments to the position of L6 are also helpful. To find the spectral peak of the signal, it is necessary to take a spectrum at fixed delay by scanning the monochromator. If the maximum does not correspond to the desired wavelength of PL, the nonlinear crystal must be rotated to adjust the phase matching. This normally requires a few iterations of rotation, tweaking, and taking a spectrum.

The experiment itself is simple to execute, if somewhat time consuming. Because of the low signal levels, the PMT counts were monitored in 30 second bins for each delay. A few data points were acquired at negative delay to establish a baseline for the data. The delay was spaced in a logarithmic manner, so that the density of points was high at short delays, where the signal changes rapidly, and much lower at long delay, where the signal decreases slowly. Because the PMT dark count level was time dependent, a background was taken after each data point by blocking the excitation beam. The temperature is usually controlled to within 0.1 K. This consists mostly of adjusting the liquid nitrogen flow into the sample chamber to keep a constant level. The best temperature stability was achieved when the liquid nitrogen level was above the bottom of the sample probe but well below the sample. A typical data run consists of about 30-50 points and takes about 1.5 hours.

Chapter 4

Results and Discussion

4.1 CW spectra

The 77K cw luminescence spectrum for our thin film PPV sample is plotted in Figure 4.1. The data presented in this section have not been corrected for the spectral response of the system. The highest peak at 533 nm results from a purely electronic transition from the first excited state (S_1) to the singlet ground state (S_0), and is usually denoted as the $S_1 \rightarrow S_0/0 \rightarrow 0$ transition [1]. The $0 \rightarrow 0$ notation, used here to indicate a zero-phonon transition, indicates the vibrational levels involved in the process. The peak at 563 nm and the shoulder at 610 nm are attributed to the phonon-assisted $S_1 \rightarrow S_0/0 \rightarrow 1$ and $S_1 \rightarrow S_0/0 \rightarrow 2$ transitions, respectively. These transitions occur between the ground vibrational level of the excited state S_1 and the n th vibrational level of the ground state. The relatively strong, vibrationally-assisted transitions are a manifestation of the strong coupling between the photo-excited electron-hole pairs and the nuclear configuration of the molecule.

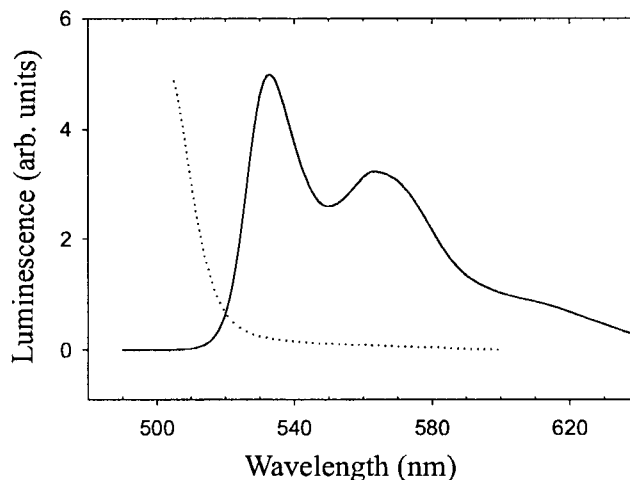


Figure 4.1: Photoluminescence spectrum of a thin film of PPV at 77K (solid line) shown with room temperature absorption edge (dotted line).

The delocalization of π electrons along the chain is important for the semiconducting behaviour of conjugated polymers. In a given bulk sample, the range of effective conjugation lengths produces an inhomogeneously broadened density of states (DOS) distribution [2] that gives rise to the relatively broad lines evident in the luminescence spectrum. The temperature dependent luminescence spectra are shown in Figure 4.2. The spectra have been normalized to the same peak value and offset for clarity. It should be noted that the highest energy peak may be red-shifted somewhat due to its proximity to the absorption edge (shown in Figure 4.1).

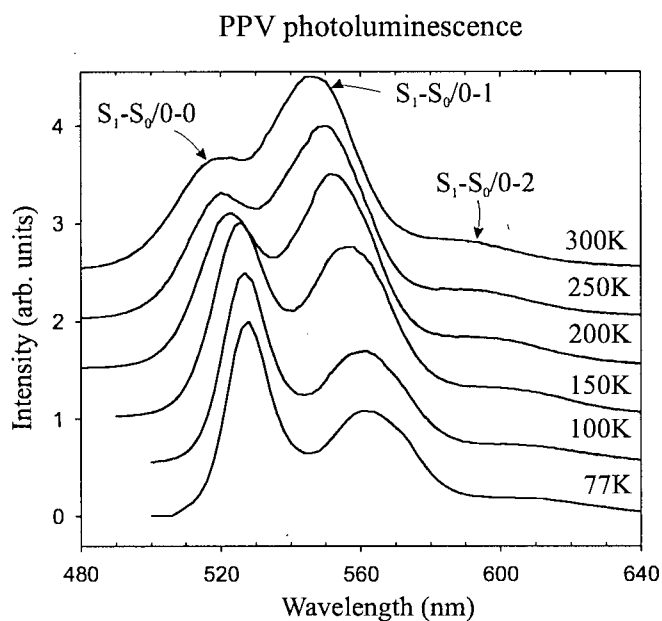


Figure 4.2: Temperature dependence of PPV photoluminescence. The data were normalized to the same peak value and offset for clarity.

With increasing temperature, the separation of the first vibrational transition (one-phonon replica) decreases with respect to the pure electronic transition as the polymer backbone becomes less rigid. The red shift of the peaks with cooling has been attributed to the freezing out of torsional modes of the phenylene rings [1], resulting in a longer effective conjugation length and a lower emission energy.

4.2 Time resolved spectra (77 K data)

In order to study the excitation dynamics, the PPV photoluminescence at 77K was time resolved using the upconversion technique described in Chapter 3. The short time scale regime is plotted in Figure 4.3. The zero delay is not known exactly, but is defined for these plots as the position of the first data point above the noise. The data are plotted on intermediate (0-100 ps) and long (0-600 ps) time scales in Figures 4.4 and 4.5. From these plots we can see evidence of two distinct regimes in the data: a fast decay, which occurs within 20 ps, followed by a slower tail which extends to several hundred picoseconds. The data that decrease monotonically with delay were fit phenomenologically to a biexponential of the form

$$I = I_0 + w_1 e^{-t/t_1} + w_2 e^{-t/t_2}, \quad (4.1)$$

where I_0 is a constant background, t_1 and t_2 represent the short and long time constants, respectively, and w_1 and w_2 are the respective weighting factors. The offset I_0 effectively accounts for the contribution from PL on nanosecond time scales, as has been observed by many authors [3, 17, 18]. The fits are shown superimposed on the data in Figure 4.5, and reproduce the data effectively.

From the fits, the two time constants at 77K were extracted and plotted with the cw luminescence, as shown in Figure 4.6. The fast time constant becomes faster with increasing energy until, for the highest energy data set, it is not observable within the time resolution of our system. By contrast, over the 40 nm range of data, the long

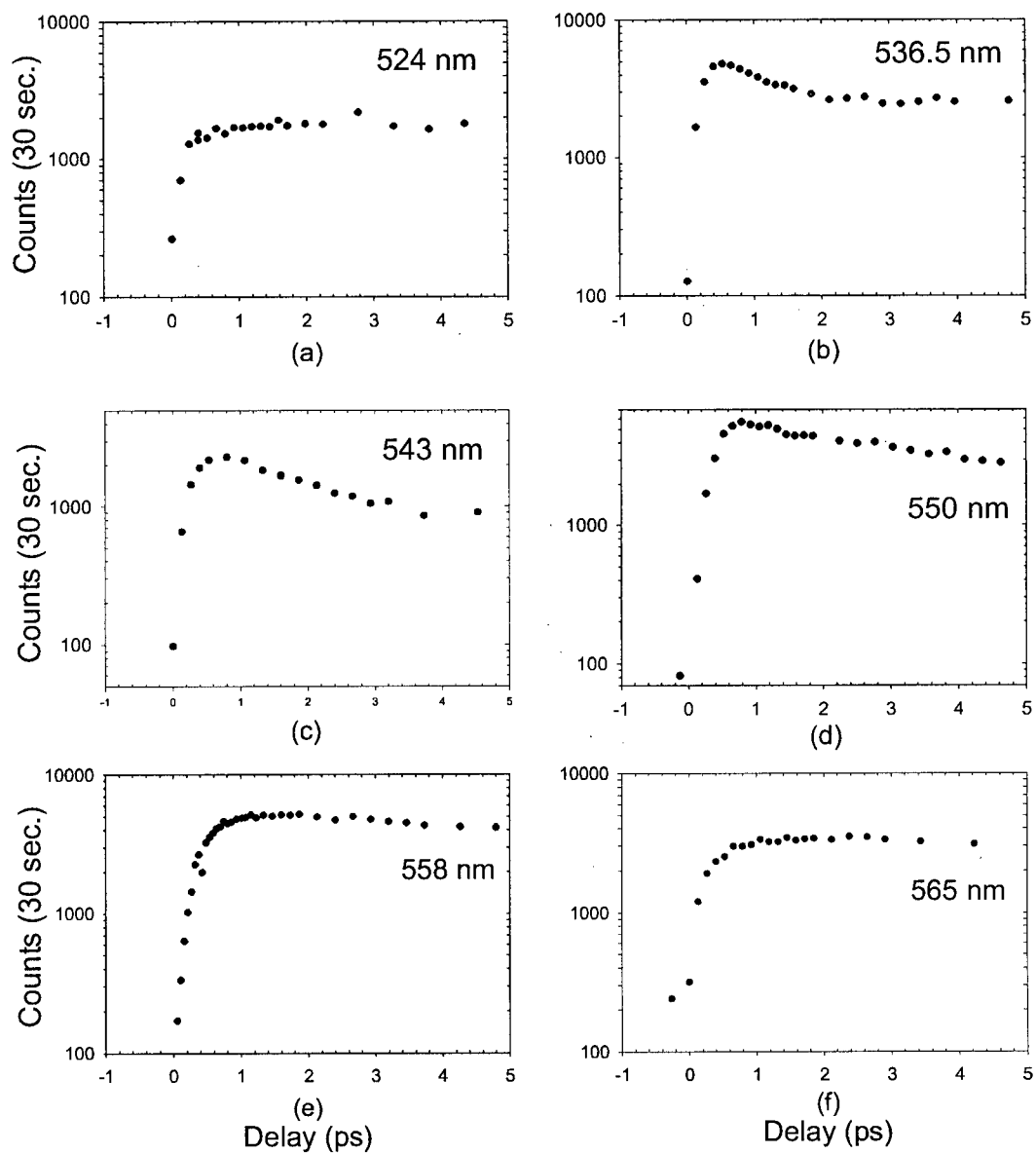


Figure 4.3: Short time regime of upconverted PPV luminescence at 77K.

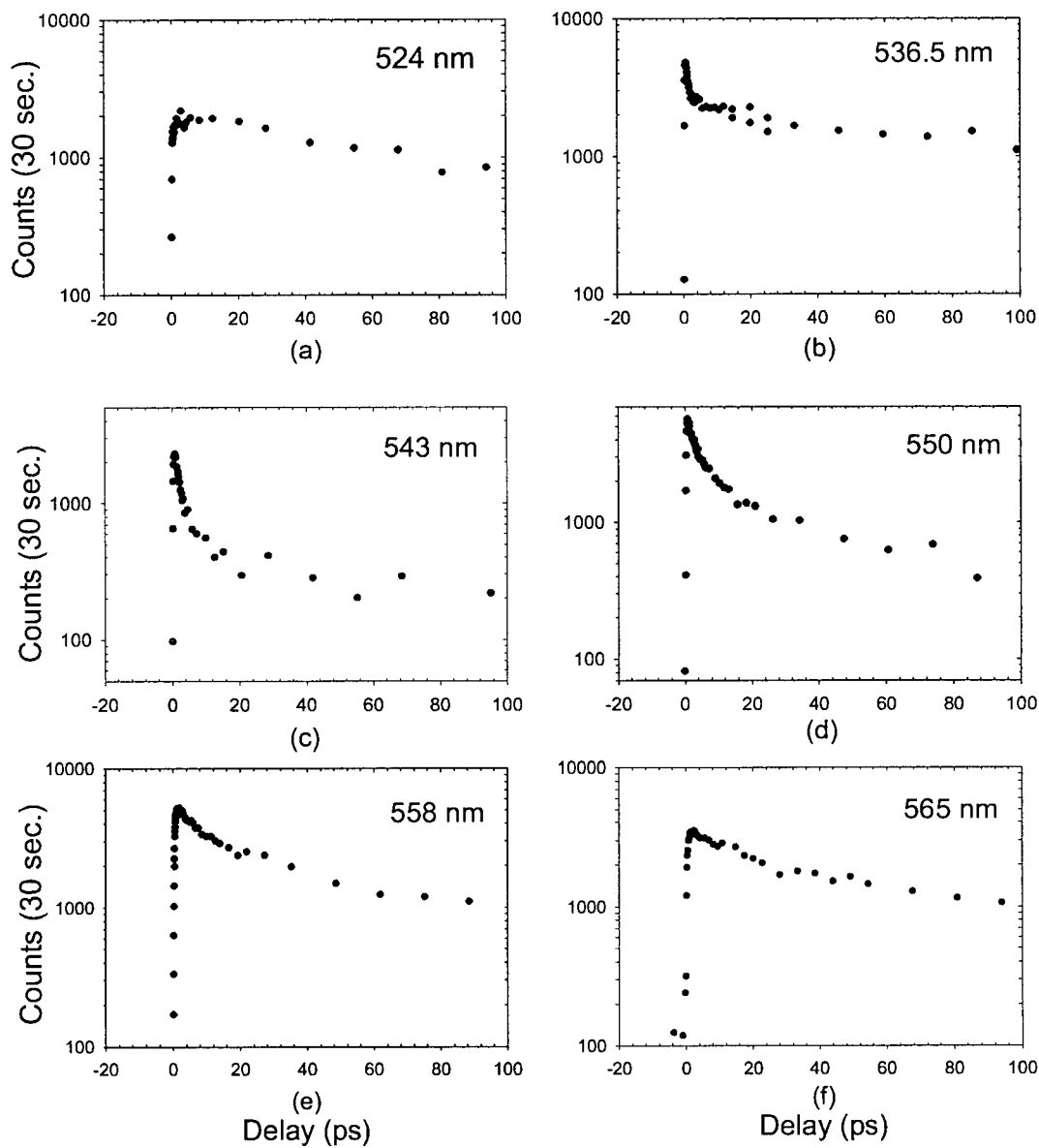


Figure 4.4: Intermediate time regime of time resolved PPV luminescence at 77K.

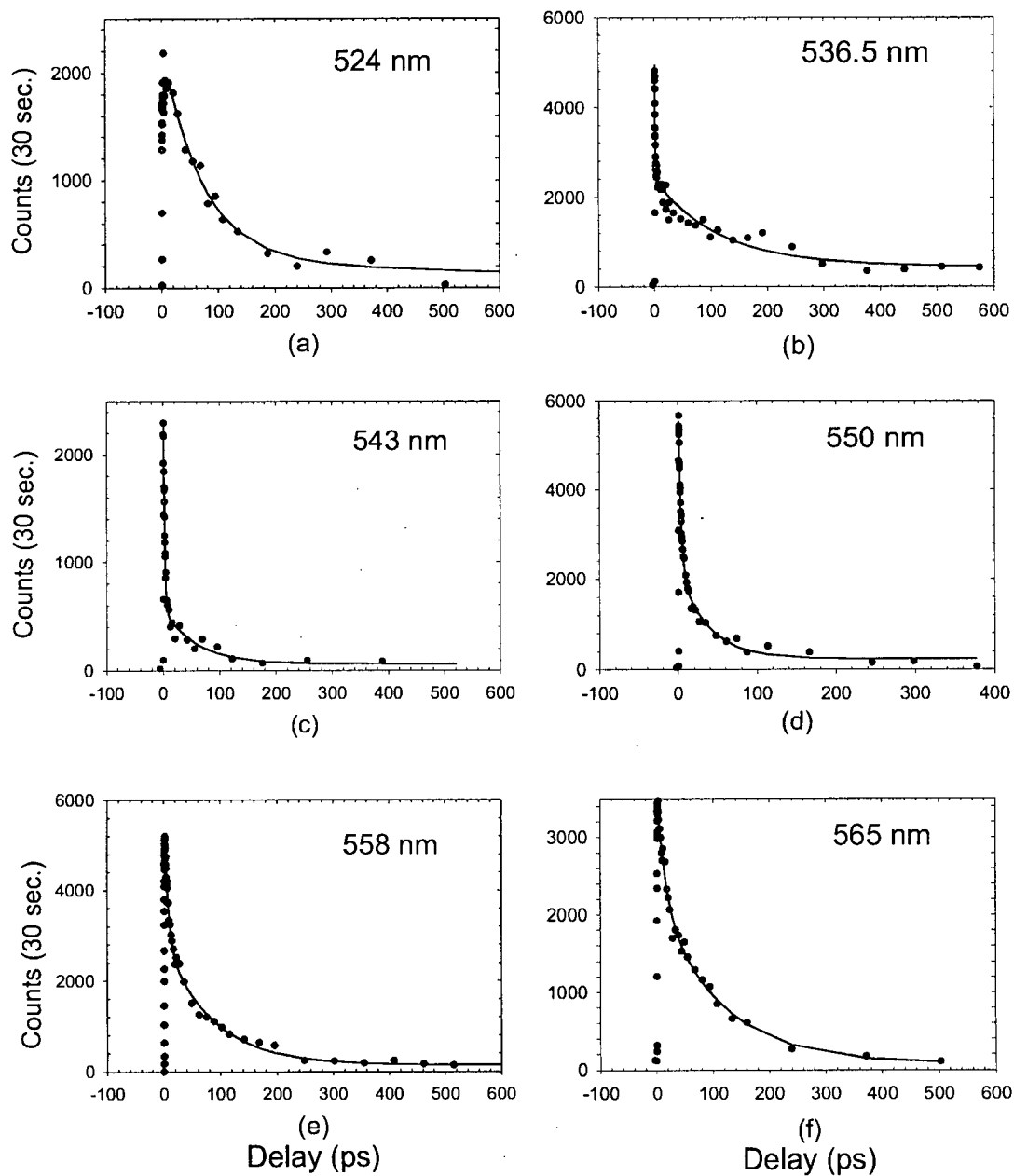


Figure 4.5: Long time scale regime of upconverted PPV luminescence at 77K. The solid lines represent biexponential fits.

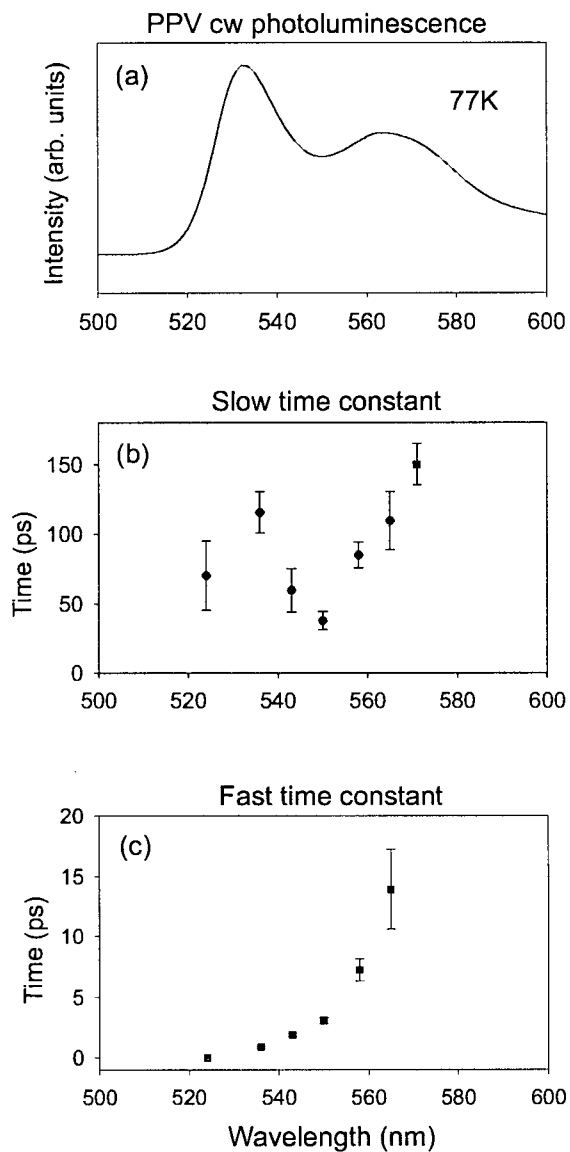


Figure 4.6: The 77 K cw luminescence spectrum (a) is shown with the slow (b) and fast (c) time constants extracted from the biexponential fits of Figure 4.5. The two time constants exhibit markedly different spectral behaviour. The square in (b) is an estimate of the time constant from the 2.17 eV data of Hayes et al. [19].

time constant appears well correlated to the luminescence peaks. It is longest at the luminescence maxima, and assumes its shortest value (37 ps) at 550 nm, in the valley between the zero and one-phonon transitions.

4.3 Time resolved spectra (300 K data)

For completeness, we show the room temperature results fit to the biexponential function in Figure 4.7. The decay time constants are summarized in the plots of Figure 4.8. The peak of the luminescence spectrum in Figure 4.8a corresponds to the one-phonon transition at 300K, which is blue-shifted by 18 nm (73 meV) from the same feature at 77K.

Based on the accuracy of the fits, there is evidence of two time regimes at 300K, as for the low temperature data. The slow time constant is considerably faster at room temperature than at 77K. The magnitude of the fast time constant is comparable at both temperatures. A more quantitative analysis of the 300 K results would require more data points across a greater spectral range.

4.4 Context

The most comprehensive work in this area has been undertaken by Kersting et al. [2, 3]. Their experiment on films of PPV covers a broad energy range of 2.2-3.0 eV (413-564

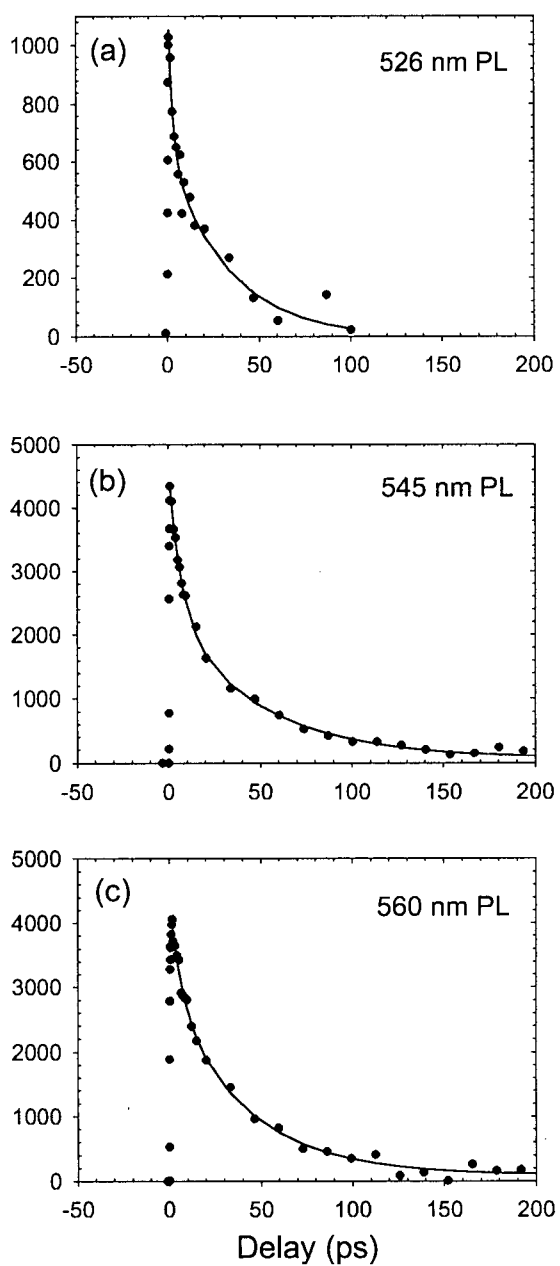


Figure 4.7: Luminescence transients at 300K fit to biexponentials.

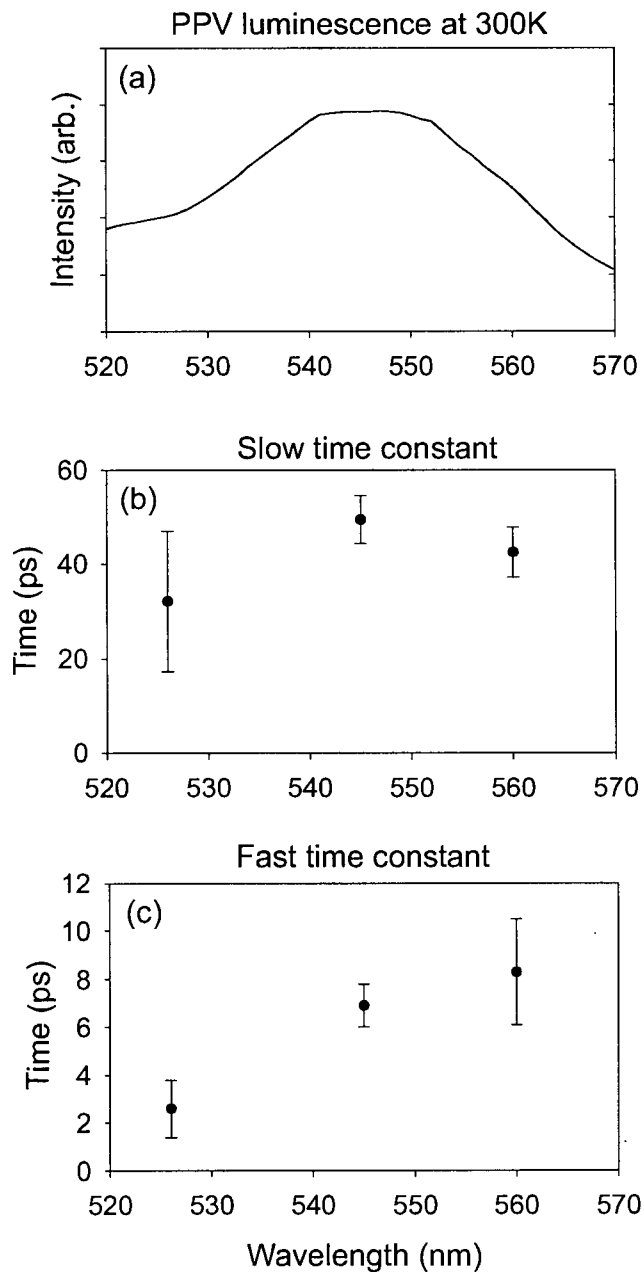


Figure 4.8: The 300K cw luminescence spectrum (a) is shown with the slow (b) and fast (c) time constants extracted from the biexponential fits of Figure 4.7.

nm) at 300 K. Their cw spectrum at 300K is very similar to our 300 K spectrum in Figure 4.2, indicating that our samples are comparable. One exception is a suppression of the $S_1 \rightarrow S_0/0 \rightarrow 2$ transition shoulder at 590 nm in our results, likely an artifact of the system response. In their 1993 paper [2], they present delayed spectra from 0-2 ps and luminescence transients over the energy range 2.4-2.7 eV (459-517 nm). They elaborate on these transients in a more detailed fashion in the 1997 paper [3], but do not explicitly extract any time constants.

Hayes et al. [19] discuss the polarization dependence of PPV photoluminescence and present some transient data of interest. From their long time evolution data at 571 nm (2.17 eV) and a temperature of 10K, a time constant of about 150 ps can be extracted from the first 200 ps of decay. Assuming the temperature effect is not too great between 10K and 77K, this is consistent with a long wavelength extrapolation of our slow time constant at 77K (see Figure 4.6b).

Samuel et al. [17] are one of the few groups to fit luminescence transients to a bi-exponential form. They are most interested in the effect of polymer conjugation on the time resolved photoluminescence. They describe transients at different emission wavelengths, and find time constants that are significantly longer than ours. For example, for 550 nm PL at 77K, they report short and long time constants of 345 ps and 1104 ps, respectively. However, the time resolution of their system is 40-50 ps, so they are not sensitive to any fast decays. Warmuth et al. [20] also present good biexponential fits, but give little mention of the extracted time constants.

4.5 Interpretation

In discussing the two time constants we have extracted, it is useful to delve further into the work of Kersting et al. [3]. They present a quantitative numerical analysis of high energy luminescence transients, from 2.4 eV to 2.7 eV. In their model, laser excitation instantly results in excitons uniformly occupying a small fraction of the states throughout the DOS. The dynamics are dictated by one of two termination processes: either the excitons migrate via spectral diffusion between energy states (i.e. jump between differently conjugated links), or they fall into trap (defect) states which are energetically positioned below the DOS, and that are presumed not to contribute to emission spectra.

The model used by the authors is based on something they call incoherent hopping of excitons. The neutral excitations randomly redistribute themselves among different polymer chains. The probability of transfer to higher energy states is limited by the exponential restriction imposed by the Maxwell-Boltzmann distribution. The initial conditions and hopping motion are governed by a Monte Carlo method, and a space-energy transport master equation solves the excitation dynamics. They attribute the luminescence dynamics to an intra-chain cascading of the excitons from high energy states to low energy states. The relaxation of high energy states is faster since there is no compensatory feeding mechanism. By contrast, the emptying of lower energy states is offset by filling from higher energy transitions.

While this model has some success for the higher energy data presented in their paper,

the 2.4 and 2.5 eV data fit quite poorly. Their model cannot account for the rapid rise in the luminescence at these energies. To explain the discrepancy, the authors speculate that the fast component is in fact due to emission associated with the high-energy tail of the one-phonon transition. Because the various phonon assisted transitions basically sample the same inhomogeneously broadened set of excitons, they modelled their lower energy decay curves by superimposing the dynamics of the nominal (zero-phonon) DOS with the dynamics associated with a part of the DOS shifted to higher energy (and hence faster), by a single phonon energy. By adjusting the relative weights of the two contributions, a reasonable fit was obtained to the lower energy data, down to 2.4 eV.

To gauge whether or not the data presented in this chapter can be explained by the Kersting model, we must first address the different spectral responses of the fast and slow time constants. Note that our data is all at lower energy than that presented by Kersting et al. In particular, it spans the zero and one-phonon peaks in the cw spectra. Figure 4.6 shows the two time constants extracted from the biexponential fits shown in Figure 4.5, as a function of emission wavelength. The fast time constant monotonically increases towards longer wavelength, while the slow time constant varies in a manner correlated with the cw emission peaks. Based on Kersting's interpretation, we believe that the fast time constant is associated with the high energy tail of the exciton DOS as sampled via the *two-phonon* transition. Because the range of wavelengths sampled is all below the peak in the two-phonon emission, there is a monotonic variation in the time constant, increasing towards the centre of the DOS.

It is tempting to associate the long time constant data at wavelengths longer than 550 nm as a redundant, double sampling of the spectral dependence of the exciton decay time in the vicinity of the peak of the DOS at 533 nm. This would imply that the decay time roughly mimics the DOS, decreasing on either side of its peak. This is not consistent with the qualitative predictions of Kersting's model for spectral diffusion. There is also an obvious inconsistency in this interpretation for the slow time constant: why are there not three time constants instead of two?

Looking at the data and fits shown in Figure 4.5, and the cw spectrum, it appears that a triple exponential might provide a better description for the data in the region between the zero and one-phonon peaks. From the plots shown in Figure 4.5, it is evident that the biexponential function fits the 536.5 nm and 550 nm data less well than at the other wavelengths. The 536.5 nm fit is poor in the range 20-100 ps, whereas the 550 nm fit is not ideal at longer delays. The 543 nm data is also spectrally positioned in the valley, but is already well described by the biexponential.

To address this issue, triple-exponential fits were applied to the 536.5 nm and 550 nm data. The fits improved, as evidenced by a decrease of more than 25% in each of the chi squared values. With this additional information, the set of time constants from the bi-exponential fits outside the spectral valley and the tri-exponential fits in the valley are summarized in Figure 4.9. For comparison, the cw spectrum is also shown, and the horizontal axes are converted to energy units. The intermediate time constant at 2.25 eV (550 nm) essentially reproduces the short time constant, and has been omitted for clarity.

The short (solid line) and intermediate (dotted line) time constant lines are guides to the eye to facilitate the following discussion.

Figure 4.9 reinforces our fast time constant hypothesis. To show this, the fast time constant data (solid line) were translated to higher energy by 169 meV (dotted line), equal to the energy separation of the one and two-phonon peaks from the cw spectrum. There is excellent continuity between the translated fast time constant fit and the intermediate time constant fit (both shown as dotted lines). This agreement supports an interpretation of the fast time constant as a high energy two-phonon sampling of the exciton DOS. Similarly, the intermediate time constant must be viewed as a one-phonon sampling of the same DOS.

The completed one phonon trace (dotted line) was then translated a further 124 meV higher in energy (dashed line), which corresponds to the energy separation of the zero and one-phonon peaks in the cw spectrum. This shifted curve is consistent with the zero-phonon data (triangles), although the error bars are too large to give any further insight.

In view of the results from the triple-exponential fits, the non-monotonic behaviour of the slow time constant from the bi-exponential fits (Fig. 4.6) is explained as an artifact of fitting two separate time constants, corresponding to the zero-phonon and one-phonon transitions, with a single parameter. In fact, in Figure 4.9 these combined dynamics are still evident in the long time constant point at 2.25 eV, which lies midway between the zero and one-phonon curves.

We show in Fig. 4.10 an estimated Gaussian DOS based on a fit to the zero-phonon peak in the cw spectrum (FWHM = 72 meV) and the corresponding time constant we deduce for the exciton dynamics as a function of energy above the peak of the DOS. This quantitative determination of the decay time in the upper half of the inhomogeneously broadened exciton DOS has not been reported before, although it is qualitatively consistent with the time constants we deduce from the literature. Our 300 K data indicates that the time constant varies more with temperature near the peak of the DOS than at higher energies. One outstanding issue is that our data are well fit by exponential functions, which is not consistent with Kersting's model [3], and this question should be addressed in the future.

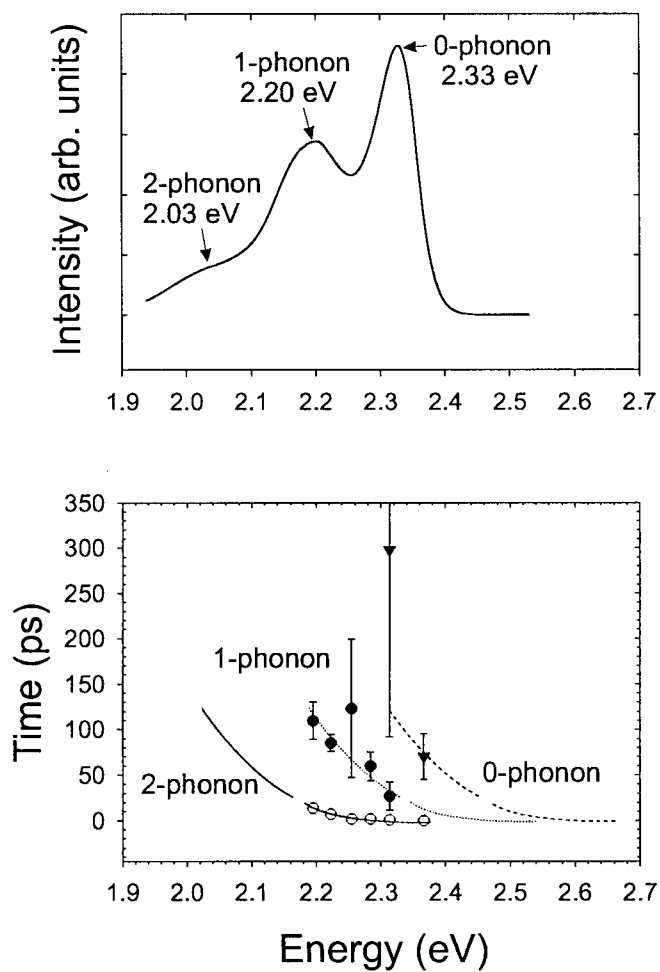


Figure 4.9: Time constants extracted from the 77 K luminescence transients. The 2.25 eV and 2.31 eV data points were extracted from triple exponential fits, while the other data are from bi-exponentials. The fits in (b) were added by hand and translated by the zero-one and one-two phonon separations measured from the cw spectrum (a) to complete the picture of the separate phonon dynamics.

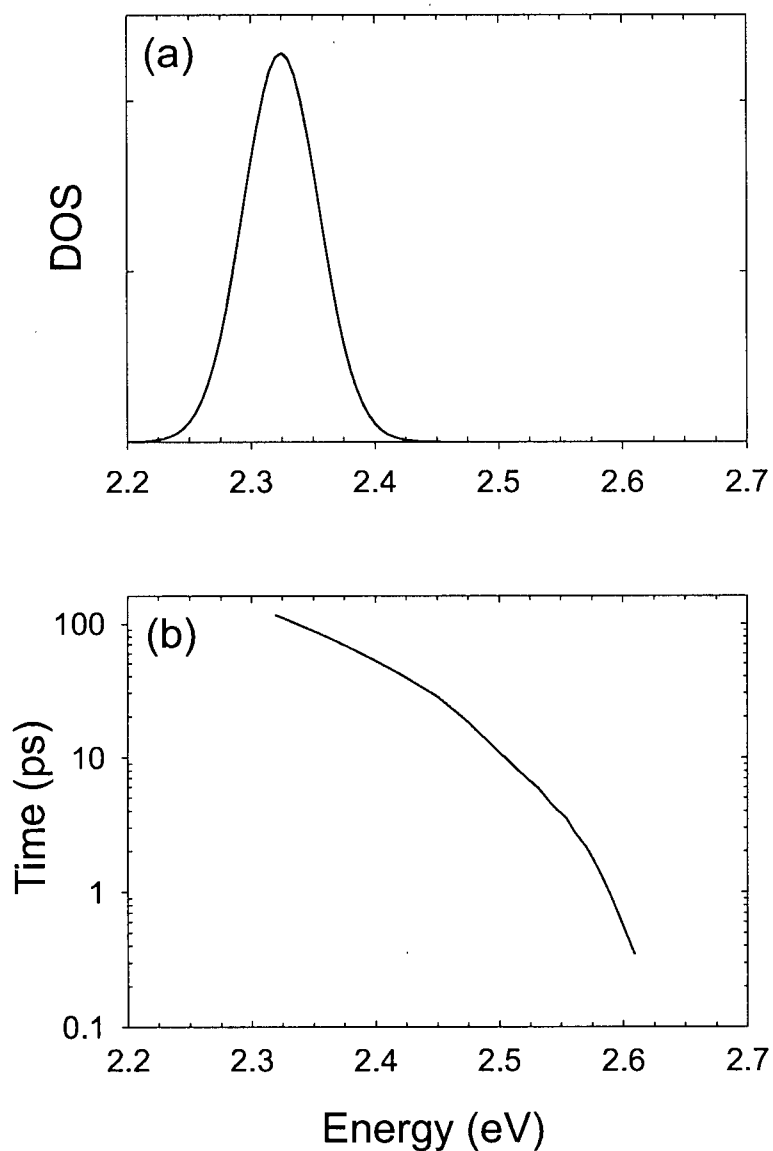


Figure 4.10: The inhomogeneously broadened exciton density of states (DOS) (a) from a Gaussian fit to the zero-phonon peak of the PL data, shown with the decay time (b) determined from fits to the luminescence transients. This quantitative result has not been previously reported in the literature.

Chapter 5

Conclusions

An optical system was successfully implemented to perform femtosecond time-resolved photoluminescence spectroscopy. Using this system, time resolved data were acquired for the conjugated polymer PPV at both 77 K and 300 K. Bi- and tri-exponential fits to the low temperature data yielded two distinct time constants: a fast time constant that decreased monotonically with increasing energy, and a slow time constant with a non-monotonic spectral dependence.

We took data at short time scales over a broader (lower) range of energies than previously discussed in detail in the literature. Borrowing the interpretation of higher energy analysis that the decay is generally a superposition of different parts of the same exciton inhomogeneously broadened DOS, as sampled by zero and one-phonon transitions, we interpret our data in terms of a superposition of two or in some cases three signals from zero, one, and two-phonon sampling of the DOS. Using this analysis, we extract from the two-phonon contribution the decay rate from 330 meV to 160 meV above the peak of the DOS. From the one-phonon contribution we get the decay rate from 109 meV above to

7 meV below the peak of the DOS. The error bars on the zero-phonon contribution are large, and cannot be used to extend the range of energies over which we extract decay times. However, the zero-phonon decay rates on the high energy side of the DOS are consistent with those extracted from the two and one-phonon transitions.

This work therefore extends considerably the range of energies over which the decay time of the inhomogeneously broadened exciton DOS is continuously measured in the same sample. The decay time increases monotonically from a value below the 300 fs time resolution of our system at an energy 330 meV above the peak in the DOS, to 116 ps at 7 meV below the peak. The decay time increases with energy faster than linearly at the highest energies, but the rate of increase becomes more linear towards the peak in the DOS. A comparison of our 300 K and 77 K results indicates that the time constant varies more with temperature near the peak of the DOS than at high energies.

We found our luminescence transients are well fit by a combination of either two or three exponential functions. This points towards a relatively simple model where the exciton dynamics are dictated primarily by non-radiative traps. This disagrees with the non-exponential, spectral diffusion model of Kersting et al., and should be addressed in future work.

Future improvements to the system are planned. The lithium iodate crystal used for sum frequency generation will be replaced by a crystal of Beta-Barium Borate (BBO) more optimally cut for phase matching PPV photoluminescence. This will allow a broader energy range of upconversion, particularly at energies above 2.4 eV, which are cut off

in the present set-up. Moreover, a crystal of BBO has significantly less group velocity dispersion than lithium iodate, yielding improved time resolution.

Cooling the photomultiplier tube to 10°C should allow reduction of the dark count level from the current 25-100 counts/sec. to <5 counts/sec. This will improve the signal to noise, allowing measurements to be taken at longer delays. Fewer dark counts will also allow each experiment to proceed faster, diminishing the consequences of signal drift or degradation.

Finally, and perhaps most importantly, reflective optics will be implemented. The elimination of the chromatic aberration from lenses should provide a large increase in the upconverted signal. A larger signal should allow operation of the monochromator in a double grating mode instead of the current single grating set-up, which will improve the energy resolution of the experiment.

Further work is required to reinforce and supplement the data in this thesis, particularly at 300 K. Implementation of these recommendations should provide a means to the acquisition of more high quality data.

From a materials perspective, the future direction of this work entails investigation of PPV encapsulated in a zeolitic host called MCM-41. The ensuing reduction of interchain interactions may help clarify the nature of the optical excitations in conjugated polymers, and may open an exciting avenue to the manufacturing of optical devices based on luminescent polymers.

References

- [1] K. Pichler, D. A. Halliday, D. D. C. Bradley, P. L. Burn, R. H. Friend, and A. B. Holmes, *Journal of Physics: Condensed Matter*, **5**, 7155, 1993.
- [2] R. Kersting, U. Lemmer, R. F. Mahrt, K. Leo, H. Kurz, H. Bassler, and E. O. Gobel, *Physical Review Letters*, **70**, 3820, 1993.
- [3] R. Kersting, B. Mollay, M. Rusch, J. Wensch, G. Leising, and H. F. Kauffmann, *Journal of Chemical Physics*, **106**, 2850, 1997.
- [4] M. Yan, L. J. Rothberg, F. Papadimitrakopoulos, M. E. Galvin, and T. M. Miller, *Physical Review Letters*, **72**, 1104, 1994.
- [5] L. J. Rothberg, M. Yan, F. Papadimitrakopoulos, M. E. Galvin, E. W. Kwock, and T. M. Miller, *Synthetic Metals*, **80**, 41, 1996.
- [6] N. T. Harrison, G. R. Hayes, R. T. Phillips, and R. H. Friend, *Physical Review Letters*, **77**, 1881, 1996.
- [7] G. R. Hayes, I. D. W. Samuel, and R. T. Phillips, *Physical Review B*, **52**, R11569, 1995.
- [8] Andras G. Pattantyus-Abraham, Michael O. Wolf, *MRS Conference Proceedings, Luminescent Materials*, Vol. 560, 1999.
- [9] Junjun Wu, Adam F. Gross, and Sarah H. Tolbert, *Journal of Physical Chemistry B*, **103**, 2374, 1999.
- [10] Bastard, Gerald, *Wave Mechanics Applied to Semiconductor Heterostructures*, New York: Halsted Press, 1988.
- [11] Jagdeep Shah, *IEEE Journal of Quantum Electronics*, **24**, 276, 1988.
- [12] Yariv, Amnon, *Quantum Electronics*, New York: John Wiley and Sons, Inc., 1975.
- [13] Boyd, Robert W., *Nonlinear Optics*, San Diego: Academic Press, 1992.

- [14] Dmitriev, V. G., Gurzadyan, G. G., and Nikogosyan, D. N., *Handbook of Nonlinear Optical Crystals*, Berlin: Springer, 1997.
- [15] Zernike, F. and Midwinter, J. E. *Applied Nonlinear Optics*. New York: John Wiley and Sons, 1973.
- [16] F. Papadimitrakopoulos, K. Konstadinidis, T. M. Miller, R. Opila, E. A. Chandross and M. E. Galvin, *Chem. Mater.*, **6**, 1563, 1994.
- [17] I. D. W. Samuel, B. Crystall, G. Rumbles, P. L. Burn, A. B. Holmes, and R. H. Friend, *Synthetic Metals*, **54**, 281, 1993.
- [18] M. Yan, L. J. Rothberg, F. Papadimitrakopoulos, M. E. Galvin, and T. M. Miller, *Physical Review Letters*, **73**, 44, 1994.
- [19] G. R. Hayes, I. D. W. Samuel, and R. T. Phillips, *Physical Review B*, **56**, 3838, 1997.
- [20] Ch. Warmuth, A. Tortschanoff, K. Brunner, B. Mollay, H. F. Kauffmann, *Journal of Luminescence*, **76 & 77**, 498, 1998.

Appendix A

Phasematching code

Below is the Maple code used to determine the phasematching angle of the nonlinear crystal for sum frequency generation. Refer to Figure A.1 for the discussion which follows the code.

```

restart;
n02:=proc(x);          # ordinary index squared for LiIO3
  3.40109 + 0.0525/(x^2-0.021865);
end:
ne2:=proc(x);         # extraordinary index squared for LiIO3
  2.91359 + 0.03712/(x^2-0.01940);
end:
lambdaG:=0.800:
lambdaPL:=0.550:

phasematch:=proc(thetar)
  local kPL, kG, kS, nS,
  thetaM, lambdaS, theta2i, theta1i, alpha, beta, theta2t, gamma, thetam;
  lambdaS:=(1/lambdaG + 1/lambdaPL)^(-1);      # sum frequency beam
  theta1i:=thetar*Pi/180;
  theta2i:=theta1i - 22*Pi/180;
  theta2t:=arcsin(-sin(theta2i)/sqrt(n02(lambdaG)));
  theta1t:= arcsin(-sin(theta1i)/sqrt(n02(lambdaPL)));
  alpha:=theta2t - theta1t;
  kPL:=sqrt(n02(lambdaPL))/lambdaPL:          # PL beam wavevector
  kG:=sqrt(n02(lambdaG))/lambdaG:            # Gate beam wavevector

```

```

kS:=sqrt(kPL^2 + kG^2 - 2*kPL*kG*cos(Pi-alpha));      # Sum beam
nS:=kS*lambdaS;                                       # Index of sum ray
beta:=arccos((-kPL^2 + kG^2 + kS^2)/(2*kG*kS));
thetam:= -44.51*Pi/180 + beta - theta2t;

(sin(thetam))^2 -
(1/nS^2-1/n02(lambdaS))/(1/ne2(lambdaS)-1/n02(lambdaS));

end:

fsolve(phasematch(thetar)=0,thetar);   #Solve numerically for thetar

```

The first statements for n_{o2} and n_{e2} are Sellmeier's equations determining the values of n_o^2 and n_e^2 for a LiIO_3 crystal at a wavelength x given in microns (taken from [11]). Next the wavelengths for the gate and PL beams are defined in microns.

The *phasematch* procedure is written as a function of θ_r (thetar), and must be solved numerically. Angles above the normal are treated as positive, and those below the normal as negative. Therefore, the angles switch signs after refraction at the interface of the crystal. All angles are converted to radians in the program. The PL beam approaches the crystal at an angle $\theta_{1i} = \theta_r$ to the normal, where θ_r represents the angle the crystal is rotated in a counter-clockwise direction. The incident angle of the gate beam is defined to be about 22° below θ_{1i} , but this must be changed if the optics are moved.

First we solve for angle $\alpha = \theta_{2t} - \theta_{1t}$ using Snell's law. Then we use the cosine law on the triangle formed by wavevectors \vec{k}_{pl} , \vec{k}_g , and \vec{k}_s to calculate \vec{k}_s , the sum frequency wave vector. The index n_s follows easily. We use the cosine law again to find angle β . This allows a calculation of $\theta_m = -44.51 + \beta - \theta_{2t}$, which is the angle that \vec{k}_s propagates

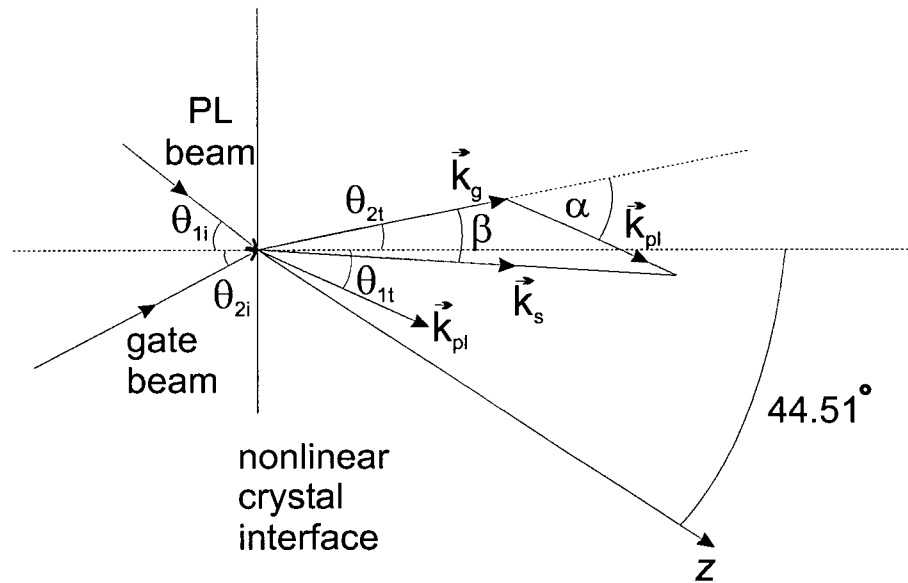


Figure A.1: Geometry for the calculation of the phasematching angle.

with respect to the optic axis of the crystal.

The final statement of the procedure is exactly equation 2.15 with all the terms taken to one side. We solve this equation (using *fsolve*) numerically for θ_r , which tells how much the crystal must be rotated to achieve phasematching.

The procedure is easily modified to calculate phasematching for second harmonic generation. Simply set $\theta_{2i} = \theta_{1i}$ and $\lambda_{pl} = \lambda_g$ so that the incident beams are collinear and the same wavelength.